Portland State University
PDXScholar

Geology Faculty Publications and Presentations | Geology

10-2014

GPS Constraints on the Mw = 7.5 Ometepec Earthquake Sequence, Southern Mexico: Coseismic and Post-Seismic Deformation

Shannon E. Graham
University of Wisconsin - Madison

Charles DeMets
University of Wisconsin - Madison

Enrique Cabral-Cano
Universidad Nacional Autonoma de Mexico

Vladimir Kostoglodov
Universidad Nacional Autonoma de Mexico

Andrea Walpersdorf
Universite de Grenoble

See next page for additional authors

Let us know how access to this document benefits you.

Follow this and additional works at: http://pdxscholar.library.pdx.edu/geology_fac

Part of the Geology Commons, and the Geophysics and Seismology Commons

Citation Details

Graham, S. E., DeMets, C., Cabral-Cano, E., Kostoglodov, V., Walpersdorf, A., Cotte, N., & ... Salazar-Tlaczani, L. (2014). GPS constraints on the Mw = 7.5 Ometepec earthquake sequence, southern Mexico: coseismic and post-seismic deformation. Geophysical Journal International, 199(1), 200-218.

This Article is brought to you for free and open access. It has been accepted for inclusion in Geology Faculty Publications and Presentations by an authorized administrator of PDXScholar. For more information, please contact pdxscholar@pdx.edu.

Authors
Shannon E. Graham, Charles DeMets, Enrique Cabral-Cano, Vladimir Kostoglodov, Andrea Walpersdorf, Nathalie Cotte, Michael Brudzinski, Robert McCaffrey, and Luis Salazar-Tlaczani

This article is available at PDXScholar: http://pdxscholar.library.pdx.edu/geology_fac/52

Geophysical Journal International

Geophys. J. Int. (2014) **199,** 200–218
GJI Geodynamics and tectonics

doi: 10.1093/gji/ggu167

GPS constraints on the $M_w = 7.5$ Ometepec earthquake sequence, southern Mexico: coseismic and post-seismic deformation

Shannon E. Graham,[1] Charles DeMets,[1] Enrique Cabral-Cano,[2] Vladimir Kostoglodov,[2] Andrea Walpersdorf,[3] Nathalie Cotte,[3] Michael Brudzinski,[4] Robert McCaffrey[5] and Luis Salazar-Tlaczani[2]

[1]*Department of Geoscience, University of Wisconsin-Madison, Madison, WI* 53706, *USA. E-mail: shannonegraham@gmail.com*
[2]*Instituto de Geofísica, Universidad Nacional Autónoma de México, Mexico City, Mexico*
[3]*Institut des Sciences de la Terre, Université de Grenoble* 1, *CNRS UMR* 5265, *F*-38041 *Grenoble, France*
[4]*Department of Geology, Miami University of Ohio, Oxford, OH, USA*
[5]*Department of Geology, Portland State University, Portland, OR, USA*

Accepted 2014 May 6. Received 2014 May 2; in original form 2013 September 28

SUMMARY

We use continuous GPS measurements from 31 stations in southern Mexico to model coseismic slip and post-seismic deformation from the 2012 March 20 $M_w = 7.5$ Ometepec earthquake, the first large thrust earthquake to occur below central Mexico during the modern GPS era. Coseismic offsets ranging from ∼280 mm near the epicentre to 5 mm or less at sites far from the epicentre are fit best by a rupture focused between ∼15 and 35 km depth, consistent with an independent seismological estimate. The corresponding geodetic moment of 1.4×10^{20} N·m is within 10 per cent of two independent seismic estimates. Transient post-seismic motion recorded by GPS sites as far as 300 km from the rupture has a different horizontal deformation gradient and opposite sense of vertical motion than do the coseismic offsets. A forward model of viscoelastic relaxation as a result of our new coseismic slip solution incorrectly predicts uplift in areas where post-seismic subsidence was recorded and indicates that viscoelastic deformation was no more than a few per cent of the measured post-seismic deformation. The deformation within 6 months of the earthquake was thus strongly dominated by fault afterslip. The post-seismic GPS time-series are well fit as logarithmically decaying fault afterslip on an area of the subduction interface up to 10 times larger than the earthquake rupture zone, extending as far as 220 km inland. Afterslip had a cumulative geodetic moment of 2.0×10^{20} N·m, ∼40 per cent larger than the Ometepec earthquake. Tests for the shallow and deep limits for the afterslip require that it included much of the earthquake rupture zone as well as regions of the subduction interface where slow slip events and non-volcanic tremor have been recorded and areas even farther downdip on the flat interface. Widespread afterslip below much of central Mexico suggests that most of the nearly flat subduction interface in this region is conditionally stable and thus contributes measurable transient deformation to large areas of Mexico south of and in the volcanic belt.

Key words: Time-series analysis; Space geodetic surveys; Seismic cycle; Transient deformation; Earthquake dynamics.

1 INTRODUCTION

Extending more than 1000 km along Mexico's Pacific coast, the Mexico subduction zone (MSZ) accommodates northeastward subduction of the Rivera and Cocos plates beneath the southern edge of North America (Fig. 1). Since 1900, an average of four $M \geq 7$ earthquakes have ruptured this subduction zone every decade, including the $M = 8.2$ 1985 Acapulco earthquake that caused 10 000 or more deaths and billions of dollars of damage (Anderson *et al.* 1989; National Earthquake Information Center catalogue). Given the frequency of damaging earthquakes along the MSZ and the hazard they pose to nearly all areas of Mexico south of and within the volcanic belt, it is paramount to better understand the factors that dictate the buildup and release of strain in this region.

The focus of this paper is the most recent large thrust earthquake along the MSZ, the $M_w = 7.5$ 2012 March 20 Ometepec earthquake (Fig. 1), which damaged or collapsed roughly 8000 structures in southern Mexico and caused significant shaking in Mexico City ∼300 km to the north (UNAM Seismology Group 2013). The 2012 Ometepec earthquake was the first large thrust earthquake along

© The Authors 2014. Published by Oxford University Press on behalf of The Royal Astronomical Society.

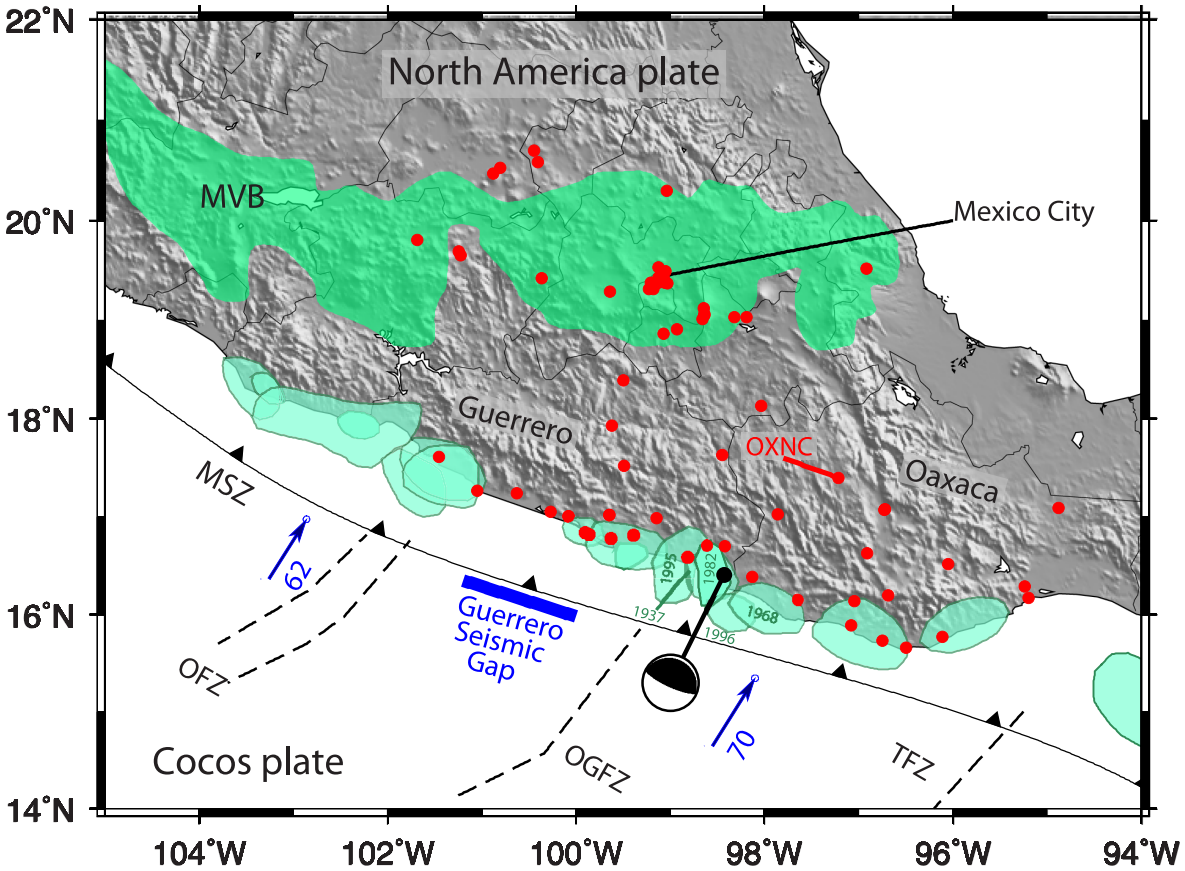

Figure 1. Tectonics and geography of the study area. Cyan patches show the rupture areas of major 20th century subduction earthquakes along the Mexico subduction zone (MSZ). Blue vectors show Cocos Plate velocities in mm yr^{-1} relative to the North America Plate (DeMets *et al.* 2010). Red circles denote locations of GPS sites. Green area shows the Mexican volcanic belt (MVB). Focal mechanism is the global centroid-moment-tensor for the 2012 March 20 Ometepec earthquake (Ekström *et al.* 2012). Dashed lines show traces of the Orozco (OFZ), O'Gorman (OGFZ) and Tehuantepec (TFZ) oceanic fracture zones near the trench.

the Cocos-North America segment of the MSZ to be recorded by enough continuous GPS stations to model in detail the pre-seismic, coseismic and post-seismic deformation. In addition, it was the first earthquake on the MSZ to occur in close proximity in space and time to a slow slip event (SSE; Graham *et al.* 2014). The earthquake thus affords the first opportunity to study the spatial relationship between three of the four possible processes by which strain is released during the MSZ earthquake cycle, namely, SSEs, coseismic rupture and earthquake afterslip, excluding only non-volcanic tremor (NVT).

Modelling of the GPS observations in the months before the earthquake indicates that the earthquake occurred at the leading edge of a SSE that began in late 2011 below eastern Oaxaca and propagated several hundred kilometres towards the eventual Ometepec earthquake rupture zone (Graham *et al.* 2014). The position time-series for continuous GPS station OXNC, which is located between eastern Oaxaca and the Ometepec rupture zone (Fig. 1), illustrates the sequence of events associated with the Ometepec earthquake (Fig. 2). Prior to early 2012, the site moved steadily towards the North America Plate interior, reflecting elastic shortening of the upper plate due to interseismic coupling along the MSZ (Fig. 2). The reversal of the direction of site motion at OXNC in early 2012 recorded the arrival of slow slip that was propagating westward along the plate interface towards the area of the subduction interface that subsequently ruptured during the Ometepec earthquake. The 2012 March 20 earthquake not only moved site OXNC ~8 mm towards the rupture zone (southwards), but also

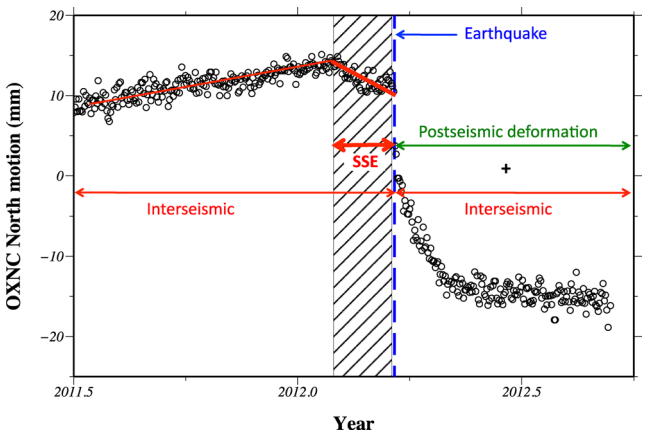

Figure 2. GPS daily position time-series for the north component of motion at site OXNC relative to the interior of the North America Plate, mid-2011 to late 2012. Before the 2012 Ometepec earthquake, the site moves steadily northward towards the plate interior, reflecting elastic shortening of the plate inland from the locked Mexico subduction zone. Transient deformation in early 2012 reflects the temporary effect of a slow slip event (SSE) propagating westward along the subduction interface below central Mexico (Graham *et al.* 2014). Motion after the earthquake consists of transient post-seismic deformation and steady elastic shortening from relocking of the subduction interface after the earthquake. North America Plate motion relative to ITRF2008 is estimated using an angular velocity that minimizes the motions of ~1300 continuous GPS stations in the plate interior relative to ITRF2008.

triggered transient post-seismic deformation whose magnitude exceeded the coseismic deformation by more than a factor of 2 within several months of the earthquake.

Herein, we use the observations from OXNC and 30 other continuous GPS stations that were operating during the Ometepec earthquake to investigate a series of questions about the MSZ earthquake cycle. Does the downdip limit for coseismic slip during the Ometepec earthquake confirm that large thrust earthquakes on the MSZ rupture down to only relatively shallow depths of 20–25 km, as indicated by aftershock distributions for previous MSZ thrust earthquakes (Suárez & Sánchez 1996; Pacheco & Singh 2010)? What proportion of the transient post-seismic deformation can be explained by fault afterslip versus viscoelastic flow in the lower crust or mantle wedge below central Mexico? If afterslip is required, where did it occur? How much of the afterslip was accommodated by aftershocks? Did the regions of coseismic slip and fault afterslip overlap each other or overlap the regions of well-documented SSEs below central Mexico (e.g. Lowry *et al.* 2001; Kostoglodov *et al.* 2003; Brudzinski *et al.* 2007; Larson *et al.* 2007; Correa-Mora *et al.* 2008, 2009; Vergnolle *et al.* 2010; Radiguet *et al.* 2012; Cavalie *et al.* 2013)? Finally, what does this earthquake teach us about the mechanical behaviour of the subduction interface below central and southern Mexico?

The paper is organized as follows: After summarizing recent research about the earthquake cycle of southern Mexico, we describe and model GPS measurements due to the coseismic and post-seismic deformation at 31 and 18 sites, respectively, in southern and central Mexico. Our modelling is focused on determining the spatial distribution of coseismic and post-seismic slip that occurred on the subduction interface. In contrast, GPS measurements after an earthquake record the net deformation attributable to fault afterslip, viscoelastic relaxation of elevated coseismic stresses within the lower crust and the mantle wedge above the subducted slab, and steady long-term interseismic locking of parts of the subduction interface. Since interseismic deformation is not of interest here, we remove its contribution to the post-seismic deformation by subtracting the interseismic motion measured at each site during the years that preceded the 2012 earthquake from each site's post-seismic motion. Viscoelastic deformation at each site is forward-modelled for a lower-crust/mantle-wedge viscosity model that maximizes the estimated viscoelastic deformation and is compared to the well-determined post-seismic measurements at each site. Time-dependent inversions of the GPS coordinate time-series that are corrected for both interseismic deformation and a maximum-response viscoelastic model are used to determine the minimum afterslip that was triggered by the earthquake. The paper concludes with a discussion of the implications of the results for the transition from locked to free slipping behaviour on the nearly flat subduction interface in southern Mexico.

2 SUBDUCTION SETTING FOR THE OMETEPEC EARTHQUAKE

At the rupture location of the 2012 Ometepec earthquake, the Cocos Plate subducts beneath North America with a velocity of 69 ± 3 mm yr^{-1} towards N31°E $\pm$ 1° (DeMets *et al.* 2010). The seismogenic area of the subduction interface thus accumulates ~7 m of thrust motion per century. During the past 50 yr, significant ruptures of this trench segment occurred in 1968 ($M_w = 7.3$), 1982 ($M_w = 6.9$ and $M_w = 7.0$) and 1996 ($M_w = 7.1$; Yamamoto *et al.* 2013). The known plate convergence can be accommodated by comparable-size ruptures every few decades assuming characteristic, average slip amplitudes of 2–5 m for such earthquakes (Pegler & Das 1996) or by larger, but more infrequent earthquakes such as the $M \sim 8.6$ earthquake that may have ruptured this segment and adjacent segments of the MSZ in 1787 (Suárez & Albini 2009).

The 2012 earthquake occurred near the midpoint (98.5°–98°W) of a ~400-km-long, linear segment of the MSZ (100°W–96°W), where 10–15-Myr-old Cocos Plate seafloor subducts at nearly right angles to the trench. There is no evidence that thickened oceanic crust has subducted in this region since at least 30 Ma (Skinner & Clayton 2011). The only fracture zone that subducts along this segment, the O'Gorman fracture zone (Fig. 1), intersects the trench ~50 km northwest of the 2012 rupture zone and plays no obvious role in the earthquake. Other factors that may influence the locations and dimensions of ruptures in this area include three NE-trending lines of seamounts that subduct along this portion of the trench (UNAM Seismologic Group 2013) and upper plate segmentation suggested by shallow microseisms in this region (Yamamoto *et al.* 2013).

More pertinent to this study, measurements from a 2-yr-long deployment of 100 broad-band seismometers in southern Mexico unambiguously show that subducted oceanic crust beneath central Mexico remains at depths of 40–50 km to a distance of 200–225 km inland from the trench, defining one of Earth's shallowest subduction zones (Perez-Campos *et al.* 2008; Kim *et al.* 2010). Although thrust earthquakes in this region appear to be confined to areas of the subduction interface that are shallower than ~25 km (Suárez & Sánchez 1996), numerous SSEs beneath central Mexico at depths of ~20–40 km have been recorded geodetically since the mid-1990s (e.g. Lowry *et al.* 2001; Kostoglodov *et al.* 2003; Brudzinski *et al.* 2007; Larson *et al.* 2007; Correa-Mora *et al.* 2008, 2009; Vergnolle *et al.* 2010; Radiguet *et al.* 2012; Cavalie *et al.* 2013; Graham *et al.* 2014). Seismic observations in southern Mexico further reveal that widespread NVT occupies a distinct source region along the subduction interface deeper than the source regions of SSEs (Payero *et al.* 2008; Brudzinski *et al.* 2010; Kostoglodov *et al.* 2010). The absence of any obvious correlation in time and space between NVT and SSE in central Mexico suggests that they represent different slip processes that arise from variations in temperature, pressure and dehydration fluids with depth along the relatively flat subduction interface (Song *et al.* 2009).

3 GPS DATA, ANALYSIS AND EXAMPLE TIME-SERIES

Our results are determined from the coordinate time-series of 31 continuous GPS stations located within and south of the Mexican volcanic belt (Fig. 1), encompassing the region affected by the Ometepec earthquake and its post-seismic deformation. Data from nearly all the stations extend several years or longer before the earthquake and 6 months (or longer) after the earthquake, as required for this work.

GPS code-phase data from each station were processed with release 6.1 of the GIPSY software suite from the Jet Propulsion Laboratory (JPL). No-fiducial daily GPS station coordinates were estimated using a precise point-positioning strategy (Zumberge *et al.* 1997), including constraints on a priori tropospheric hydrostatic and wet delays from Vienna Mapping Function (VMF1) parameters (http://ggosatm.hg.tuwien.ac.at), elevation- and azimuthally dependent GPS and satellite antenna phase centre corrections from IGS08 ANTEX files (available via ftp from sideshow.jpl.nasa.gov) and

corrections for ocean tidal loading (http://holt.oso.chalmers.se). Phase ambiguities were resolved using GIPSY's single-station ambiguity resolution feature. All daily no-fiducial station location estimates were transformed to IGS08, which conforms with ITRF2008 (Altamimi *et al.* 2011), using daily seven-parameter Helmert transformations from JPL. Spatially correlated noise between stations is estimated from the coordinate time-series of linearly moving continuous stations outside the study area and is removed from the time-series of all sites (Márquez-Azúa & DeMets 2003). Further details are given by Graham *et al.* (2014).

Uncertainties in the daily station positions are determined empirically from the day-to-day scatter of the 3-D continuous site locations with respect to station locations averaged over 30-d-long windows for each site. The daily scatter is similar for the stations in the study area, averaging ±1 mm (1σ) for station latitudes and longitudes and ±3 mm for site elevations. We use these as the daily 1σ site position uncertainties for the ensuing time-series inversions. Although uncertainties in the vertical component are larger than for the horizontal component, the coseismic and post-seismic vertical motions at many of our GPS sites are 2–20 times greater than the uncertainty in the vertical and thus contribute significantly to both the coseismic and post-seismic solution described below.

4 MODELLING METHODS

4.1 TDEFNODE

We use TDEFNODE (McCaffrey 2009) to model the spatial and temporal evolution of coseismic and post-seismic slip for the Ometepec earthquake. Within TDEFNODE, parametrized functions are used to describe the time and space distributions of slip $s(x, w, t)$ on the fault surface as a function of time t, along-strike distance x and downdip distance w, as given by

$$s(x, w, t) = A \bullet X(x) \bullet W(w) \bullet S(t), \tag{1}$$

where $s(x, w, t)$, the slip rate on the fault, is the product of the slip amplitude A, the along-strike and down-dip components of spatial functions $X(x)$ and $W(w)$ and function $S(t)$ that describes the time dependence of the slip (McCaffrey 2009). Elastic deformation is calculated within TDEFNODE using the Okada (1992) elastic half-space dislocation algorithm. Slip is constrained to be in the plane of the subduction interface. The free parameters that describe the source are estimated via a combination of a grid search and simulated annealing and are adjusted to minimize the sum of penalties and the reduced chi squared of the data misfit, (χ^2_ν), where χ^2_ν is defined as $(\chi^2)/(N-m)$ and the degrees of freedom, $N-m$, is equal to the number of observations N, minus the number of free parameters m. Penalties are applied to constrain parameter values and to apply smoothing and damping to the slip distributions. Further details on TDEFNODE are provided in the auxiliary material of McCaffrey (2009).

A cross-section that extends inland from the trench (Fig. 3) defines the geometry of the subduction interface near the mid-point of our modelling grid. Within our elastic half-space model, the subduction interface is represented by a surface that is defined by an irregular grid of node points. The depth to the interface is constructed from depth contours digitized from Radiguet *et al.* (2012), who define the subduction interface based on the seismically defined slab geometry of Pérez-Campos *et al.* (2008). Our model space extends along-strike from 94°W to 105°W and from the surface to 80 km depth. Fault nodes are spaced 5 km along-strike and 3 km downdip in the plane of the fault.

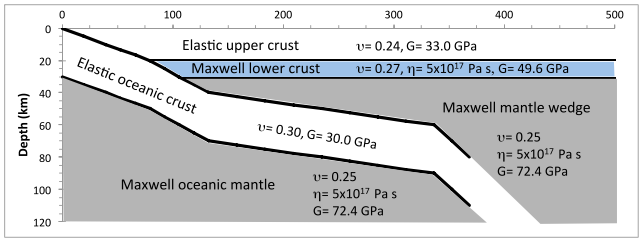

Figure 3. Depth cross-section of the study area extending inland from the Mexico subduction zone, including the geometry of the subduction interface used for our elastic half-space model and the layers and properties for the viscoelastic modelling described in the text. Values for Poisson's ratio (υ) and the shear modulus (G) are adopted from Correa-Mora *et al.* (2008). The layer viscosities (η) are selected to maximize the viscoelastic deformation at the surface.

During the coseismic modelling, the data we fit are the north, east and vertical components of the instantaneous offsets that occurred during the earthquake. In contrast, the transient post-seismic deformation is constrained by fitting the daily 3-D position time-series for each GPS station. Both are described below.

4.2 Model resolution

We tested the resolving power of the GPS network in central Mexico via two checkerboard tests, one with patchy coseismic slip (Fig. S1a), and a second that presumes widespread post-seismic fault slip from the trench to areas inland as far as 200 km (Fig. S1b) Synthetic 3-D displacements were created for two presumed GPS networks, one consisting of all 31 sites where coseismic offsets were measured and the other limited to the 18 sites where transient post-seismic motion was measured. The synthetic offsets were then perturbed by random noise typical of GPS data and were inverted using the same smoothing value as for the preferred models for coseismic and post-seismic slip that are described in Sections 5 and 6.

The inversion results are instructive. The model based on an inversion of offsets for all 31 sites recovers most aspects of its input model (compare Figs S1a and S1c), including an area of shallow slip between the trench and coast (Fig. S1a). In contrast, an inversion of the offsets at only the 18 sites fails to recover most of the shallow slip (Fig. S1e). Both models recover the first-order features of the slip below the coast and areas farther inland, although some loss of resolution occurs due to the sparse station coverage near the centre of the network. Slip at the downdip end of the starting models is well recovered.

5 SLIP DURING THE 2012 MARCH 20 OMETEPEC EARTHQUAKE

5.1 Coseismic offsets

Offsets from the Ometepec earthquake were detected at 31 continuous GPS sites throughout southern Mexico, well distributed with respect to the rupture zone (Table 1, Fig. 4). Ideally, coseismic offsets would sample motion that spans as short an interval as possible after the earthquake, particularly at stations near the earthquake where rapid afterslip may cause significant station motion within hours of an earthquake. Due to hardware problems, our offsets instead sample modestly different time intervals. At the three sites nearest the earthquake (MRQL, OMTP and PINO located in Fig. 4), only

Table 1. Coseismic offsets estimated from GPS observations described in text.

			Observed coseismic offsets (mm)					
Site ID	Longitude	Latitude	East	σ	North	σ	Vertical	σ
ACAP	260.14	16.82	0.5	3.2	−0.7	1.2	−2.5	4.0
ACYA	260.1	16.84	−1.1	5.4	−0.7	2.8	−11.5	13.6
CAYA	259.73	17.05	0.1	2.8	1.1	1.7	−10.8	10.9
CCHO	260.94	19.38	1.4	0.8	−2.1	1.6	−7.2	7.6
DEMA	260.96	20.3	3.2	6.0	−1.3	1.0	−0.2	5.8
DOAR	260.35	17.02	3.2	6.0	−1.3	1.0	−0.2	5.8
HUAT	263.89	15.77	−1.1	2.3	0.3	1.2	−5.6	5.5
ICEP	261.81	19.03	−0.6	1.4	−4.0	1.5	2.9	6.2
IGUA	260.5	18.39	0.2	2.3	−1.4	1.1	−4.8	5.8
MEZC	260.38	17.93	−1.7	1.5	−3.1	1.5	0.3	6.0
MMX1	260.93	19.43	0.1	0.9	−1.1	0.7	−10.3	3.6
MOGA	258.77	19.65	0.5	1.8	−0.8	1.6	−2.0	5.4
MRQL	261.18	16.59	−29.7	4.9	−10.1	4.1	−5.6	17.2
OAX2	263.28	17.08	−6.6	0.7	−4.1	1.8	−0.6	3.3
OMTP	261.58	16.7	−44.5	3.1	−279.0	3.0	−112.3	7.3
OXAC	261.96	18.13	−2.5	2.3	−10.2	4.2	−2.1	5.8
OXEC	263.95	16.52	−2.6	1.9	−2.1	3.1	−1.1	5.9
OXGU	263.09	16.63	−8.8	2.5	−2.1	1.7	−0.1	15.3
OXLP	262.95	16.14	−0.5	6.1	−0.8	2.2	0.8	9.9
OXNC	262.78	17.4	−8.4	3.3	−8.2	3.1	−3.4	8.7
OXPE	262.92	15.89	0.7	2.6	0.7	1.5	5.3	6.7
OXTP	261.55	17.63	−2.2	1.2	−18.9	7.8	−5.8	6.4
OXTU	262.35	16.15	−4.7	2.0	−3.6	1.2	−11.8	6.0
PINO	261.87	16.39	−105.3	3.0	−75.0	3.1	−37.9	8.1
TOL2	260.36	19.29	−0.3	1.3	−0.6	1.2	−4.8	2.9
UCOE	258.31	19.81	2.0	2.5	−0.1	2.3	−5.5	4.6
UIGF	260.82	19.33	1.3	1.4	−0.2	2.3	1.4	5.8
UNIP	260.82	19.31	0.5	0.9	−1.6	0.9	0.5	8.9
UXAL	263.08	19.52	2.3	3.4	−2.0	0.6	−0.6	6.1
YAIG	260.93	18.86	2.2	3.3	−3.8	0.6	5.4	10.9
ZIHP	258.54	17.61	0.6	0.8	0.1	1.5	−8.7	7.0

PINO was operating during the earthquake. Its offset is estimated from its 3-D position change during the days before the earthquake and 6 hr of data after the earthquake. Site OMTP ceased recording data 12 min before the earthquake and did not resume recording until 7 hr after the earthquake. Its offset thus samples post-seismic deformation that occurred during roughly 10 hr after the earthquake. Site MRQL ceased operating the day before the earthquake and did not resume recording until 2 d after the earthquake. Its estimated coseismic offset is thus biased by 2 d of post-seismic deformation.

We estimated the contributions of post-seismic deformation to the coseismic offsets measured at OMTP and MRQL by extrapolating the logarithmic-decay curves for their post-seismic time-series back to the time of the earthquake (Section 6.3.1). Post-seismic deformation at site OMTP is predicted to account for approximately 9, 2 and 3 per cent of the observed east, north and vertical components of the measured coseismic offset, respectively. At MRQL, the predicted post-seismic motion during the 2 d before this station began operating after the earthquake equals approximately 20, 35 and 4 per cent of the observed east, north and vertical coseismic displacements, respectively. As is described in Section 5.2, the effect of these biases on our estimated coseismic slip solution is small enough to ignore for the remainder of the analysis.

Other sites more remote from the rupture zone have offsets that are based on at least 6 hr of data immediately after the earthquake. At sites where post-seismic deformation was not observed and where coseismic offsets were small (typically less than 10 mm), several days of data before and after the earthquake were used to reduce the uncertainties in their pre- and post-earthquake positions. Horizontal offsets range from 283 ± 4 mm at site OMTP near the earthquake epicentre to less than 5 mm at sites farther than 300 km from the epicentre (Fig. 4). Vertical offsets range from 112 ± 7 mm of subsidence directly inland from the rupture to negligible values farther inland (Fig. 5c and Table 1). The offsets determined from our GPS measurements confirm offsets that were independently estimated from accelerograph measurements at sites PINO, MRQL and OMTP (shown in fig. 9 of UNAM Seismological Group 2013).

5.2 Coseismic slip solution and its updip and downdip limits

Using TDEFNODE, we inverted the 31 coseismic offsets to estimate a best-fitting coseismic slip solution. Displacements were fit with eq. (1) while employing an impulse function for $S(t)$ and independent fault nodes with smoothing to derive the spatial distribution of slip [i.e. $X(x)$ and $W(w)$]. We began by testing the fit for an assumed coseismic slip source defined by a 2-D Gaussian slip distribution. With a weighted root-mean-square (WRMS) misfit for this model of 8.2 mm and reduced chi-square of 9.3, the misfits were roughly a factor of 3 larger than the average assigned uncertainty.

We thus explored alternative slip sources, whereby the slip amplitude at each node and a single, uniform rake are estimated during the inversion. We tested several smoothing types and found that spread smoothing, where slip is penalized for distance from the slip centroid, worked the best for the coseismic inversion. Fig. S2(a) shows the trade-off between the model variance and assigned smoothing

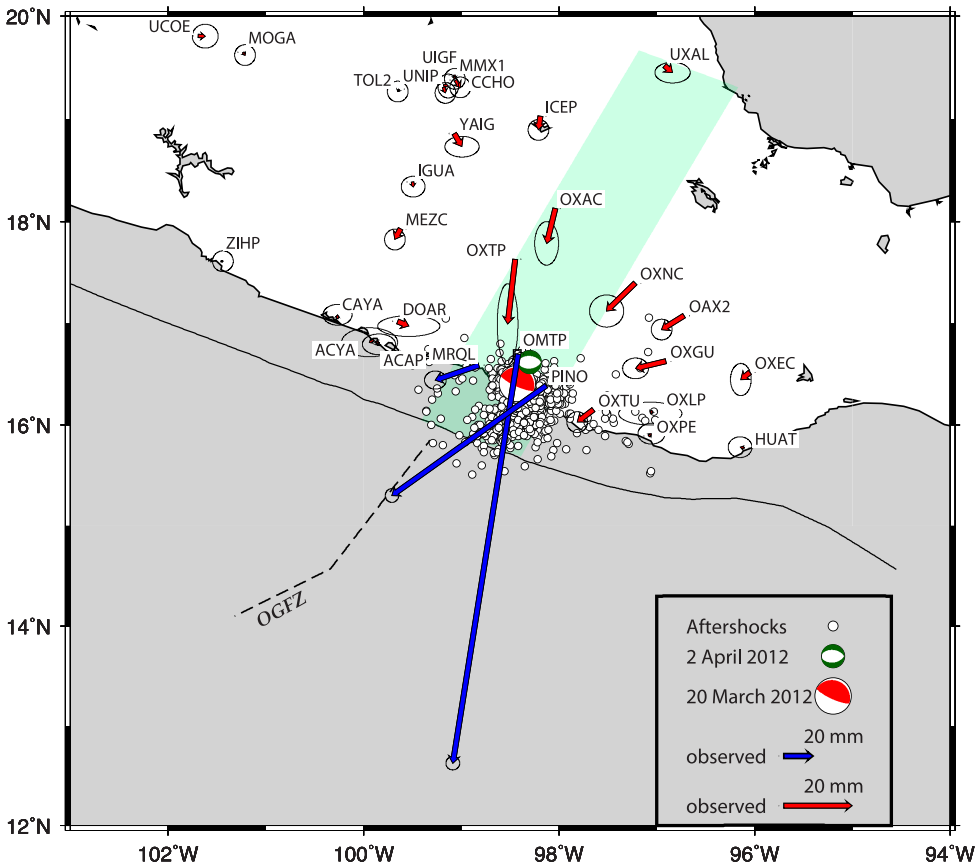

Figure 4. Coseismic offsets, focal mechanism and aftershocks for the 2012 March 20 Ometepec earthquake at GPS sites in central and southern Mexico. (a) Horizontal offsets and their 2-D, 1σ uncertainties. The offsets shown by the blue and red arrows use different scales, as shown in the figure legend. Green focal mechanism shows the April 2 ($M = 6.0$) intraslab normal faulting aftershock. Aftershocks for the four weeks after the earthquake (white circles) are from the Servicio Sismilogico Nacional catalogue. The green-shaded region defines the trench-normal transect for which vertical offsets are shown in Fig. 5.

parameter, which we use as the basis for selecting a smoothing parameter. The best-fitting slip solution is robust with respect to modest changes in the smoothing factor. Varying the slip azimuth through a plausible range gave a best value of 25°, falling between the azimuths estimated for the global CMT (21°) and the U.S.G.S CMT (31°) and close to the N31°E convergence direction predicted at this location (DeMets *et al.* 2010).

Most of the observed offsets are fit well (Figs 5a–c), with a WRMS misfit of 2.7 mm and reduced chi-square of 2.05. However, the offsets at sites inland from the earthquake are systematically overestimated by our coseismic model (Fig. 5a), possibly because the GPS offsets at sites OMTP and MRQL are upward-biased by post-seismic deformation (Section 5.1). We tested the degree to which our coseismic slip solution might be affected by the post-seismic biases in the offsets measured at these two sites by inverting coseismic offsets at OMTP and MRQL that were reduced by the amounts stated in Section 5.1 and the original coseismic offsets for the other 29 sites. We found, however, no significant change in either the coseismic slip solution (only a 4 per cent reduction in maximum slip amplitude) or fit to the data relative to the preferred solution shown in Fig. 5. Any post-seismic contribution to the offsets thus has little effect on the estimated coseismic slip solution. We attribute the remaining small misfits variously to our homogeneous elastic half-space assumption, uncertainties in the geometry of the subduction interface, possible monument or ground instability at some GPS sites during the earthquake and random errors.

Our best-fitting coseismic slip solution is dominated by an elongate 30 × 50 km region of 2.5 to 4.7 m of slip centred at 16.5°N, 98.5°W and includes areas of lesser coseismic slip (0.25–1.0 m) that extend downdip to depths of ∼35 km and east of the main slip area (Fig. 5b). The coseismic slip appears to have been concentrated downdip from the 10 km subduction contour (Figs 5a and b). Checkerboard test results for the stations used in the coseismic slip inversion demonstrate that any slip updip of the 10-km subduction contour would be detected. The apparent absence of slip updip from a depth of 10 km is further supported by two lines of evidence. First, the offsets at near-source sites PINO, OMTP and MRQL (Fig. 4) strongly constrain the location of the slip and require a slip centroid somewhere between rather than updip from the three sites. In particular, the WSW-pointing offset at site MRQL is in a near-nodal location with respect to the rupture centroid and cannot be satisfied by a slip centroid located substantially outboard from the coast. Second, aftershocks associated with the rupture were concentrated strongly downdip from the 10 to 15 km isodepth contour and inversions of near-source and far-field displacements determined from seismic observations also place nearly all the slip at depths below ∼10 km (UNAM Seismological Group 2013).

The estimated geodetic moment, 1.42×10^{20} N·m ($M_w = 7.37$) agrees well with respective W-phase moment estimates of 1.3×10^{20} and 1.4×10^{20} N·m from UNAM (UNAM Seismological Group 2013) and the U.S. Geological Survey, but is 25 per cent smaller than centroid-moment tensor estimates of 1.8×10^{20} N·m from the

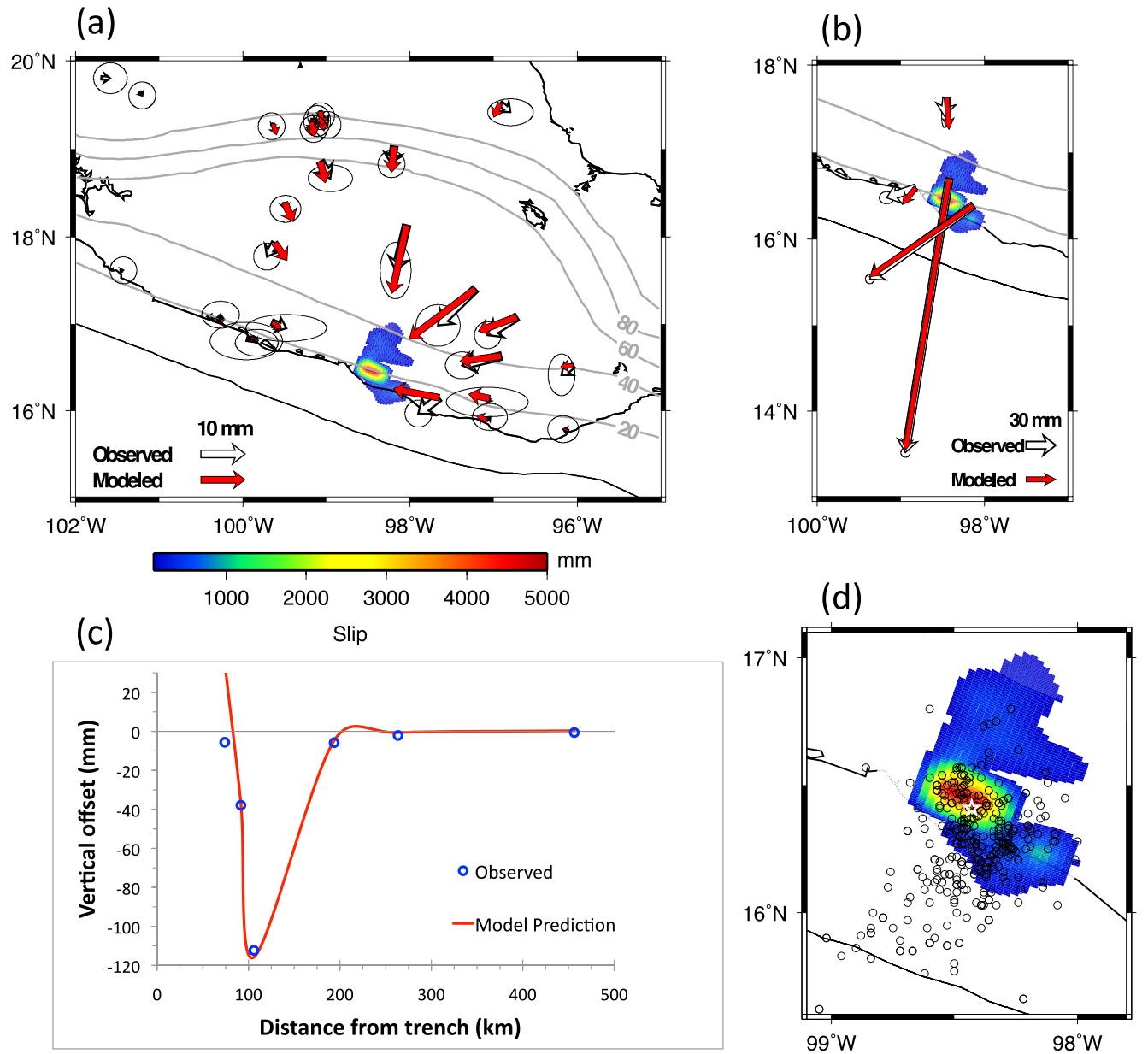

Figure 5. Coseismic modelling results. (a) Best-fitting coseismic slip solution and fits to horizontal coseismic offsets at far-field GPS sites. White and red arrows show observed and modelled GPS offsets, respectively. (b) Observed (white) and modelled (red) coseismic offsets for GPS sites close to the earthquake. (c) Observed (circles) and modelled (red line) vertical coseismic offsets for six stations located within the trench-normal transect identified in the previous figure. (d) Close-up of coseismic slip solution with aftershocks.

U.S. Geological Survey and 2.0×10^{20} N·m from Ekström *et al.* (2012). The source of these discrepancies is unknown.

We tested the limits on both the deepest and shallowest coseismic slip that are required to fit the data via a series of inversions where we systematically preclude slip on an increasing number of rows of fault nodes up dip or down dip of the 20 km isodepth contour (where slip is centred). The resultant fit to the data for each inversion demonstrates the necessity of slip at a given depth on the interface. If we forbid any coseismic slip at fault nodes shallower than 20 km, the misfit to the data increases greatly relative to our preferred slip solution, thus indicating that slip shallower than 20 km is required in order to fit the observations. Gradual improvements in the fit occur as we add nodes closer to the trench, however allowing slip on nodes shallower than ~16 km depth does not change the fit to the data. Slip at depths less than 16 km is therefore not required to fit the observations.

For the downdip limit, inversions that forbid slip on nodes deeper than 25 km increase the misfit by more than 30 per cent relative to the preferred solution, implying that coseismic slip extended below 25 km. Gradual improvements to the fit occur as we add progressively deeper nodes, but the fit stops improving for models with nodes deeper than 30 km. Slip below 30 km is therefore not required to fit the observations. The GPS data are thus well fit by models that limit coseismic slip to areas of the subduction interface between depths of 16 and 30 km.

6 POST-SEISMIC DEFORMATION: FAULT AFTERSLIP OR VISCOUS FLOW IN THE MANTLE AND LOWER CRUST?

To first order, deformation that follows large earthquakes is a superposition of steady interseismic strain from locked areas of the subduction interface, frictionally controlled fault afterslip and viscoelastic relaxation of the elevated coseismic stresses in the lower crust and upper mantle. Separating the contributions from the latter two processes is challenging given the numerous unknowns, including but not limited to the appropriate crust–mantle rheology to apply, the viscosity structure, the geometry of deeper areas of subduction faults and the uncertain location, magnitude and temporal characteristics of fault afterslip (e.g. Hu & Wang 2012; Wang *et al.* 2012). For some earthquakes such as the $M_w = 8.0$ 1995 Colima-Jalisco subduction earthquake, fault afterslip and viscoelastic deformation give rise to significantly different deformation patterns that permit both processes to be detected in the post-seismic deformation observations (Márquez-Azúa *et al.* 2002). We investigate the potential contribution of each below, beginning with forward calculations of the maximum likely viscoelastic response and concluding with calculations of lower and upper bounds for the fault afterslip.

6.1 Continuous GPS observations

During the first 6 months after the 2012 Ometepec earthquake, 18 cGPS sites recorded post-seismic transient motion, consisting of movement of all sites towards the rupture zone (Fig. 6a), uplift at stations within 100 km of the coast (Fig. 6c) and deformation that decayed with time after the earthquake (Figs 6b and S4). Due to hardware problems, the three sites nearest the earthquake, MRQL, OMTP and PINO all failed at varying points after the earthquake. Despite significant gaps in their time-series (Fig. S4), all three sites operated for at least 2–3 months immediately after the earthquake, during the period of rapid post-seismic deformation that is the most critical for modelling afterslip.

The pattern of post-seismic deformation differs from the coseismic pattern in three important respects. First, the sense of vertical deformation changed from coseismic subsidence at sites near the rupture to post-seismic uplift (Fig. 6c). Second, the directions of post-seismic movement at sites near the rupture zone changed by as much as 20° relative to their coseismic offset directions (compare light blue and dark blue arrows in Fig. 6a). Finally, the gradient in horizontal deformation changed. The 6-month cumulative post-seismic offsets at sites 150 km or farther inland were two to three times larger than their coseismic offsets (Fig. 6d and compare red and open arrows in Fig. 6a), whereas cumulative post-seismic offsets for sites closer to the rupture zone were only 0.5–2 times larger than their coseismic offsets (Fig. 6d and dark and light blue arrows in Fig. 6a).

The 18 GPS sites whose time-series record the post-seismic deformation are well distributed with respect to the earthquake (Fig. 6a), suggesting that they can be used to determine the relative contributions of afterslip and viscoelastic deformation to the post-seismic deformation. Below, we model all 18 GPS position time-series with a combination of forward and inverse calculations. Prior to fitting the position time-series, we removed the influence of steady interseismic strain at each GPS site by correcting its daily site positions for the movement that is predicted from each site's pre-earthquake velocity. The corrected time-series should be dominated by deformation from fault afterslip and/or viscoelastic deformation.

6.2 Calculations of viscoelastic deformation

6.2.1 Assumptions and methodology

We begin by calculating an upper bound for how much viscoelastic deformation may have been triggered by the 2012 earthquake, both to evaluate whether viscous flow is a plausible source of the short-term post-seismic deformation and as a basis for estimating a lower bound on the amount of fault afterslip (in Section 6.3). Estimating an upper bound on the contribution of viscoelastic processes is relatively straightforward. To first order, the viscoelastic deformation rate at a given time after an earthquake is determined by the viscosity or viscosities that are assumed for the lower crust and mantle, and the depths, thicknesses and rheologies that are assigned to those layers. For a simple Maxwell rheology, the mantle strain rate $\dot{e}$ depends linearly on stress σ. The effective viscosity $\eta = \sigma/\dot{e}$ thus remains constant with time and surface deformation rates decay exponentially. In contrast, for a power-law rheology, the mantle strain rate is proportional to the stress and the effective viscosity thus increases with time as mantle stresses are relaxed via viscous flow (Burgmann & Dresen 2008; Wang *et al.* 2012). The progressive increase in the effective viscosity for a power-law rheology causes post-seismic deformation rates to diminish more rapidly than for a simple Maxwell rheology. By implication, for a given starting viscosity, the simpler Maxwell rheology maximizes the deformation per unit time and is the basis for our calculations below.

The finite element mesh that we used to predict viscoelastic deformation in central Mexico (Fig. 3) includes two elastic layers, the upper continental crust and subducting oceanic slab and three Maxwell-rheology viscoelastic layers, the lower continental crust, mantle wedge and oceanic mantle. To maximize the viscoelastic deformation, we assigned the lowest plausible viscosity, 5×10^{17} Pa s, to all three viscoelastic layers. This viscosity is based on Hu & Wang's (2012) analysis of short-term post-seismic deformation from the 2004 Sumatra earthquake, which suggests that the mantle wedge behaves as a bi-viscous Burgers body with a long term, steady state viscosity of 10^{19} Pa s and transient short term viscosity of 5×10^{17} Pa s. Viscoelastic calculations are completed with Defmod, an open source finite element code designed for modelling crustal deformation (Ali 2014).

6.2.2 Viscoelastic results

Figs 6(c) and 7 show forward calculations of the time-dependent and time-integrated viscoelastic deformation based on the finite element model described above and our best-fitting coseismic slip solution. The maximum-response viscoelastic model badly misfits the numerous, well-determined observations. For example, the model predicts slow subsidence at sites near the rupture zone such as MRQL and OMTP, where rapid post-seismic uplift is instead observed (Figs 6c and 7b). At these sites and sites farther from the rupture zone, the viscoelastic model predicts maximum horizontal offsets integrated over 6 months that are generally 10 per cent or less of the observed offsets (Fig. 7). If the viscosities of any of the three viscoelastic layers that are included in our model are higher than the lowest-case estimates we use and/or their rheologies are transient (e.g. Wang *et al.* 2012), the viscoelastic deformation would be an even smaller percentage of the measured deformation.

We conclude that the post-seismic deformation is dominated by another process, most likely fault afterslip. Below, we estimate upper and lower bounds for fault afterslip from time-dependent inversions

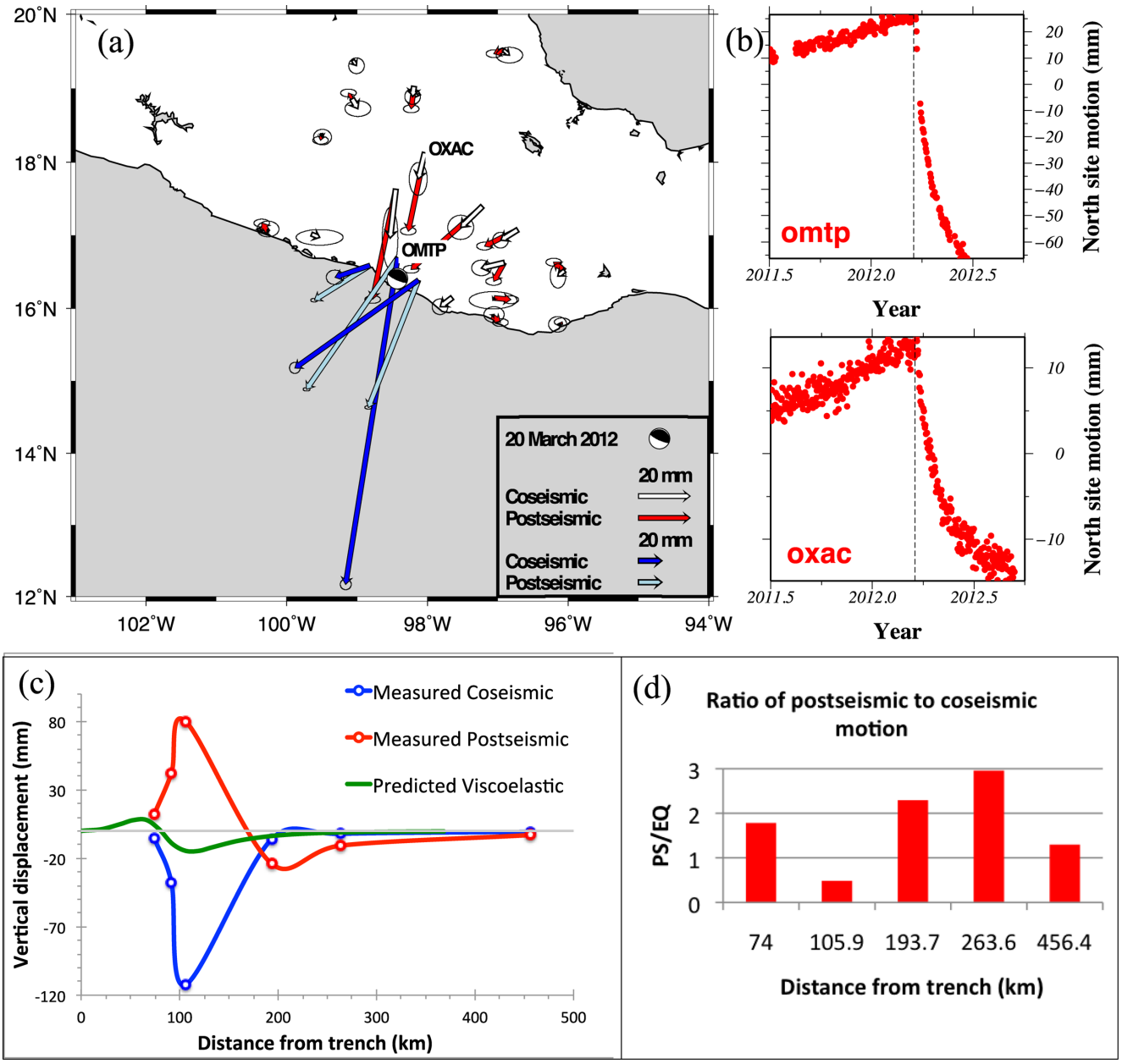

Figure 6. (a) Comparison of cumulative post-seismic motion measured within 6 months of the earthquake (light blue and red arrows) to the measured coseismic offsets (white and dark blue arrows). (b) North component of the daily position time-series for GPS sites OMTP and OXAC through 6 months after the earthquake. Red circles indicate the daily site position. Each time-series is corrected for its offset during the earthquake (indicated by the vertical dashed lines). Station locations are denoted in (a). (c) Observed vertical coseismic offsets (blue line) and post-seismic offsets (red line) for sites within the trench-normal transect defined in Fig. 4. Predictions of the viscoelastic model described in the text are shown by the green curve. (d) Ratio of horizontal post-seismic (PS) to coseismic (EQ) motion for sites in the trench-normal transect.

of two sets of GPS position time-series, one without any correction for possible viscoelastic deformation and the other corrected for the time-dependent, viscoelastic deformation that is predicted by our maximum-response viscoelastic model.

6.3 Calculations of fault afterslip

6.3.1 Methodology and afterslip decay constant

We estimated fault afterslip during the 6 months after the Ometepec earthquake using eq. (2), which imposes logarithmic decay on the fault afterslip (Marone *et al.* 1991).

$$\vec{u}_j^{\,n,e,d}\left(t_i - t_{\mathrm{eq}}\right) - v_j^{n,e,d} \cdot \left(t_i - t_{\mathrm{eq}}\right) = A_j^{n,e,d} \cdot \ln\left[1 + \left(\frac{t_i - t_{\mathrm{eq}}}{\beta}\right)\right]. \tag{2}$$

In (2), u is the position vector for the north, east or vertical component (n, e, d, respectively) at time t_i for the jth GPS site, v_j is the interseismic velocity per year for the n, e and d components, $t_i - t_{\mathrm{eq}}$ is the amount of time since the earthquake, A_j is the amplitude for the n, e and d components and β is the decay constant. We estimated the interseismic velocities v_j from GPS measurements that

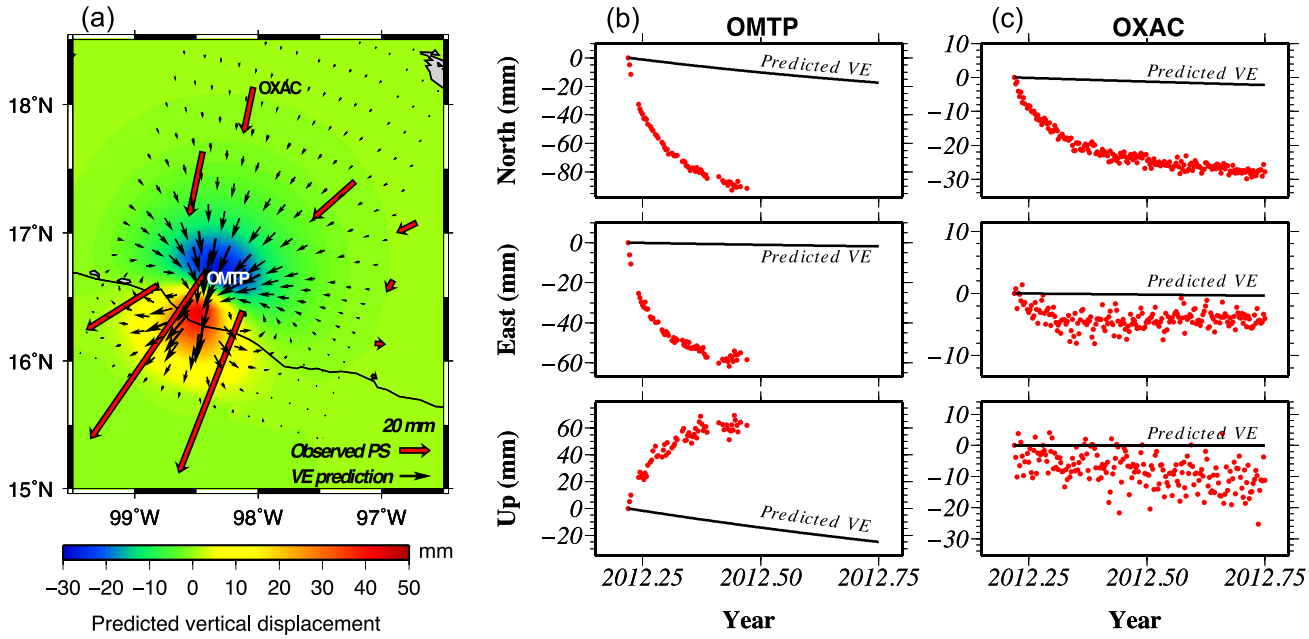

Figure 7. Predictions of the maximum-deformation viscoelastic model described in the text during the first 6 months after the Ometepec earthquake. (a) The cumulative measured horizontal offsets during this period are indicated by the red arrows in. The predicted maximum horizontal viscoelastic offsets (black arrows) are 10 per cent or less of those observed. (b, c) Predicted viscoelastic deformation (black lines) compared with the observed position time-series for the north, east and vertical components of the motions of near-field site OMTP (b) and far-field site OXAC (c). In addition to badly underestimating the magnitude of the measured motion, the viscoelastic model also incorrectly predicts slow subsidence at site OMTP, contrary to the rapid uplift observed there.

pre-dated the Ometepec earthquake, including adjustments for the effects of any SSEs. We then used the secular velocity estimates to correct the GPS position time-series before inverting to estimate fault afterslip.

We also considered using an alternative model for fault afterslip based on a brittle creep rheology (Perfettini & Avouac 2004); however, they show that for post-seismic times substantially less than a characteristic relaxation time of ∼7–10 yr, their formulation reduces to that of Marone *et al.* (1991).

Prior to our TDEFNODE inversion for the magnitude and distribution of afterslip, we simultaneously inverted all 18 GPS position time-series to determine both how well they are fit when we enforce an assumption of logarithmic decay and to estimate the decay constant, β, which dictates how quickly deformation decays after the earthquake. For a series of trial decay constants that ranged from less than 1 d to 1 yr, we simultaneously estimated all 54 n, e and d amplitude coefficients in (2) and recorded the overall misfit associated with each solution. For the decay constant that minimized the least-squares misfit, $\beta = 3$ d, reduced χ^2 is 1.3. The daily station positions are thus misfit at only 1.1 times their estimated uncertainties if we impose a simple log-decay model on the temporal evolution of the transient deformation.

Based on these results, our inversion for afterslip on the plate interface during 2012 March 21 to October 1 uses a logarithmic decay time function S(t) and decay constant of $\beta = 3$ d. At various stages of the analysis described below, we also estimated the decay constant β as part of the TDEFNODE inversions. Encouragingly, best estimates for the decay constant varied insignificantly from 3 d.

6.3.2 *Afterslip results: fit of a 2-D Gaussian slip source*

We first evaluate whether the GPS time-series are well fit if the source region for post-seismic slip is constrained to obey a simple 2-D Gaussian slip source, whereby afterslip tapers outward from the central region of an elliptical source following a Gaussian distribution. We inverted the observations to simultaneously estimate the along-strike and downdip dimensions of the source region, the amplitude and β, the decay constant necessary for specifying the logarithmic decay in the post-seismic deformation. The best decay constant, 2.5 d, agreed well with the 3-d decay constant we estimated via simple fitting of the GPS station time-series (Section 6.3.1). However, in comparison to the preferred solution that we describe below, a 2-D Gaussian slip source fits the observations significantly worse, with reduced chi-square of 21.7 versus 10.0 for our preferred solution and WRMS misfit of 5.5 mm versus 3.7 mm for the preferred solution. Fig. S3 illustrates the poor fits to the time-series for an assumed 2-D Gaussian source (solid lines).

We interpret these poor fits as evidence that the afterslip source characteristics are more complex than permitted by the simple 2-D Gaussian source. Hereafter, we estimate the afterslip solutions via independent slip amplitudes at each node, with smoothing to minimize spatial gradients in the slip and a rake selected to optimize the fit (N30°E).

6.3.3 *Best-fitting afterslip results: maximum bound*

In order to estimate an upper limit for the afterslip that occurred within 6 months of the earthquake, we used TDEFNODE to invert the GPS position time-series absent any correction for possible viscoelastic deformation. The best, smoothed afterslip solution (Fig. 8) reveals afterslip along an area of the subduction interface ∼10 times larger than the earthquake source region, nearly to the area where the Cocos Plate initiates its steep descent into the mantle (Kim *et al.* 2010). Afterslip affected all of the subduction interface between depths of ∼15 and ∼50 km, extended a remarkable 220 km inland

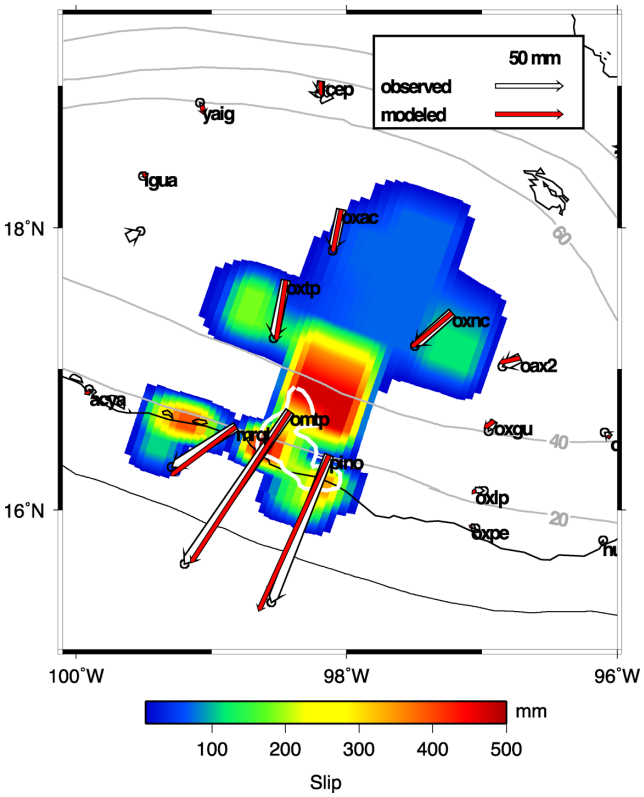

Figure 8. Best TDEFNODE solution for fault afterslip for 2012 March to October assuming that no viscoelastic deformation occurs. The white vectors show the cumulative offsets determined from the observed GPS position time-series and the red vectors show the overall surface deformation predicted by the slip solution. The cumulative offsets (white) were not used in the inversion to constrain the model. They instead show an independent comparison to deformation predicted by the best fit to the time-series. The white outline indicates the 0.5-m contour for coseismic slip. Grey lines show the isodepth contours for the subducting slab in 20 km intervals.

beneath the continent and included the entire area of coseismic slip (Fig. 8).

During the 6 months after the earthquake, the cumulative afterslip reached a maximum of 400–500 mm in areas within and immediately downdip from the rupture zone (Fig. 8). Up to ∼100 mm of cumulative afterslip also occurred at distances more than 100 km from the coast, at depths below ∼45 km. Due to the large region of the subduction interface where afterslip occurred, the cumulative, equivalent afterslip moment during the 6 months after the earthquake, 2.0×10^{20} N·m, was ∼40 per cent larger than the coseismic geodetic moment.

The best-fitting afterslip solution fits most of the GPS station position time-series within the scatter of the daily station positions (Figs 9 and S4 in the supplementary material). The WRMS misfit for the best-fitting afterslip solution is 3.7 mm, corresponding to reduced χ^2 of 10.0. Systematic misfits occur at some sites. For example, at site OMTP, where the largest post-seismic deformation occurred, the model systematically underestimates the eastward site motion by ∼5 mm (Fig. 9). At site OXAC, the logarithmically decaying afterslip misfits the curvature of the north component of the position time-series during the first month (Fig. 9). We suspect that the misfits result from the assumption that afterslip is the only source of post-seismic deformation, although some misfit may also occur due to our assumption that the afterslip decay constant is the same everywhere along the extended zone of afterslip.

6.3.4 Updip and downdip limits on afterslip location

We tested the updip limit of afterslip by precluding any afterslip from rows of nodes with depths that ruptured during the earthquake. An inversion of the 18 cGPS position time-series for such a model increases the WRMS misfit to 4.9 mm, one-third higher than for the preferred model. In particular, the poor fit of this model to the vertical time-series for site OMTP near the rupture (Fig. 10c) argues strongly for afterslip within the 2012 rupture zone. Afterslip at seismogenic depths is thus required for an acceptable fit to the observed site motions.

Given the surprising distance that afterslip extends below the continent, we also tested whether the data require afterslip that extends as far downdip as suggested by the best-fitting solution. We inverted the 18 post-seismic GPS time-series while prohibiting any afterslip on nodes located more than 150 km from the Pacific coast (corresponding to subduction interface depths deeper than 45–50 km). WRMS for this model is 3.8 mm, slightly larger than for our preferred solution (3.7 mm). The fits to the post-seismic position time-series are affected relatively little (Figs 10c–e), indicating that the penalty for restricting afterslip to a more limited area below central Mexico is small.

Although the GPS time-series are fit nearly as well by the above model as our preferred model (Fig. 8), the slip solution for the former model is less plausible (Fig. 10b). In particular, the inversion compensates for the absence of deeper slip by creating several isolated, higher-slip patches that are updip from the inland GPS sites. The slip amplitudes of these isolated patches are as much as three times that of similarly located slip in the preferred model. The fragmentation of the afterslip pattern improves some aspects of the fit (for example, the vertical fit for OXNC shown in Fig. 10d), but degrades the fit overall (as measured by the 3 per cent increase in the WRMS misfit). We tried increasing the smoothing to minimize the patchiness of this solution, but this greatly increased the misfit. The patchy slip required by the shallower-slip model thus appears to be an undesirable outcome of this model. We thus prefer the simpler afterslip solution shown in Fig. 8.

Finally, we also tested an even more restrictive model in which no afterslip is allowed on nodes below depths of 40 km, slightly deeper than the downdip limit of coseismic rupture. The WRMS misfit for this model is 4.4 mm, roughly 20 per cent greater than our preferred model. This model systematically underestimates by ∼25 per cent the afterslip recorded at sites well inland from the coast and is rejected for its poor fit to the data.

6.3.5 Afterslip results: minimum bound

In order to determine a lower bound on afterslip, we corrected the observed daily positions at all 18 GPS sites for the daily deformation predicted by our viscoelastic model (Section 6.2) during the first 6 months after the earthquake. An inversion of these modified time-series following the same procedure as for the upper-bound inversion yields a minimum afterslip solution that is nearly the same as the maximum solution, with no significant change in the WRMS misfit (3.74 mm versus 3.70 mm for the minimum- and the maximum-afterslip solutions, respectively), the afterslip amplitude (2 per cent difference), or the geographic extent of the afterslip beneath the continent or offshore. Given these results we conclude that viscoelastic deformation has little effect on our results for afterslip in the 6 months following the Ometepec earthquake.

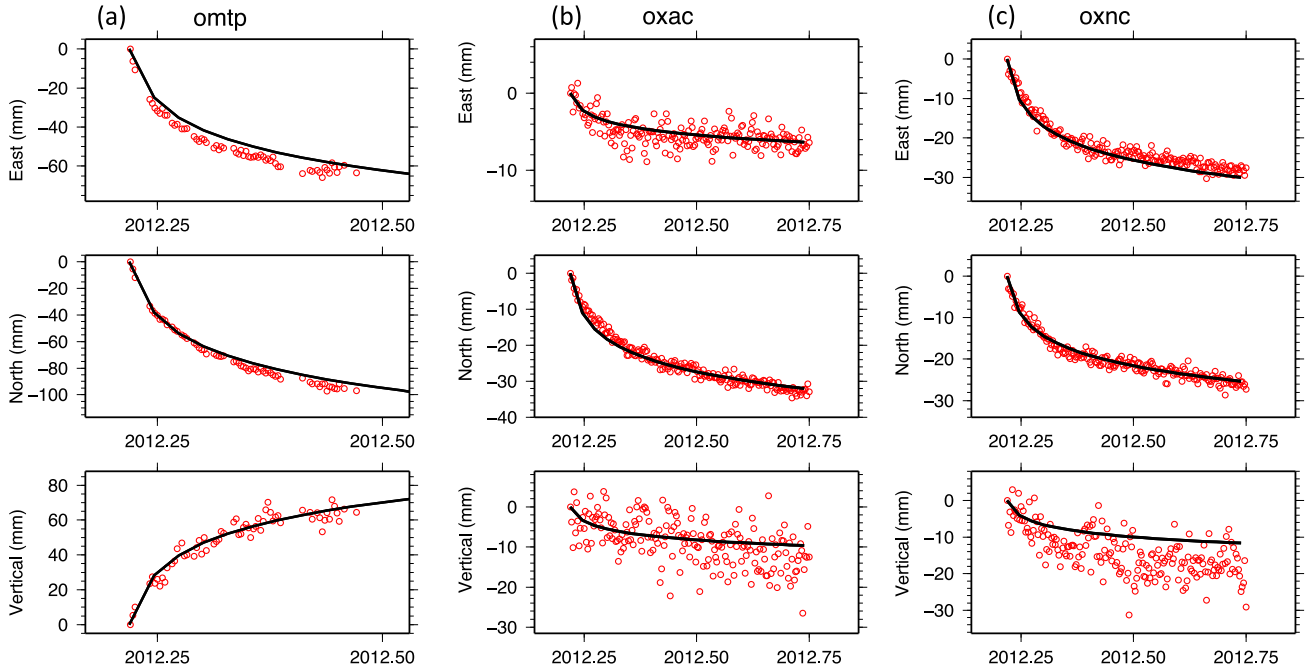

Figure 9. Fits of best afterslip solution to GPS station position time-series for (a) OMTP, (b) OXAC and (c) OXNC. Red circles show daily station positions reduced by each site's best-fitting interseismic velocity. Black line shows predictions for the preferred afterslip solution from Fig. 8. Fits to all of the time-series are shown in Fig. S4.

7 DISCUSSION

7.1 Aftershocks, coseismic slip and afterlsip: implications for the seismogenic zone

Significantly more aftershocks were recorded after the Ometepec earthquake than for other comparable size thrust earthquakes along the MSZ during the past 50 yr (UNAM Seismological Group 2013). Given that our afterslip solution predicts that 400–500 mm of fault slip occurred in regions where the aftershocks occurred (Fig. 11a), we examined whether aftershocks may have accommodated a significant fraction of the shallow post-seismic slip. During the 6 months after the earthquake, the cumulative seismic moment released by aftershocks with $M \geq 4$ was 2.5×10^{18} N·m. Our afterslip model predicts that afterslip in seismogenic areas of the subduction interface had a cumulative geodetic moment of 6.6×10^{19} N·m, during the same period. The energy released by aftershocks thus constitutes only ∼4 per cent of the afterslip geodetic moment, and aftershocks accounted for no more than 10 per cent of the post-seismic moment release at any depth (Fig. 11b). By implication, aseismic fault afterslip was responsible for most (95 per cent plus) of the post-seismic deformation along the earthquake rupture zone. These results are corroborated by our tests for the updip limit of afterslip (Section 6.3.4), where disallowing slip from the shallow portions of the fault (i.e. the seismogenic zone) greatly increases the misfit to the data.

A cross-section of coseismic and afterslip amplitudes inland from the trench (Fig. 11c) emphasizes the large difference between the two. Whereas the maximum-amplitude coseismic slip was limited to a relatively narrow area on the subduction interface (red bars in Fig. 11c), afterslip remained relatively high (between ∼50 and 100 per cent of peak slip) for ∼100 km downdip. The areas of the subduction interface below central Mexico with frictional properties that are conducive to afterslip (conditionally stable areas) thus appear to greatly exceed the areas that are conducive to seismic slip.

Our results clearly suggest that the frictional properties of the Ometepec earthquake rupture zone are heterogeneous, consisting of both velocity-strengthening and velocity-weakening patches. This is consistent with geodetic evidence for significant along-strike and downdip variations in interseismic coupling along the Oaxaca segment (97.5°–96.5°W) of the MSZ (i.e. fig. 17 in Correa-Mora *et al.* 2008), as well as for other subduction zones (e.g. Kaneko *et al.* 2010; Metois *et al.* 2012).

7.2 Shallow afterslip: implications for future earthquakes

Little apparent afterslip occurred along the subduction interface substantially updip from the earthquake rupture zone (Fig. 8), although our ability to resolve shallow afterslip is limited (Section 4.2). In addition, fewer aftershocks occurred updip from the rupture zone than in the coseismic region (UNAM Seismological Group 2013). These observations raise the question of whether the subduction interface is strongly coupled updip from depths of ∼15 km and might rupture in a future large earthquake or is instead weakly coupled and unlikely to contribute significantly to future earthquakes. Although the absence of shallow afterslip may suggest that velocity-weakening behaviour pre-dominates updip and the subduction interface is thus strongly coupled there, our ability to draw strong inferences about shallow afterslip is limited by the poorer resolution of our onshore GPS network for the shallowest areas of the subduction interface. Radiguet *et al.* (2012) estimate that the coupling coefficient along this part of the trench is moderate (0.4–0.7); however, their result is based on data from a single GPS site and is unlikely to be well resolved. We are presently modelling interseismic deformation in this region using data from many of the GPS sites used in this study (Rousset 2013). Barring evidence to the contrary, we adopt a conservative viewpoint here and conclude that the 2012

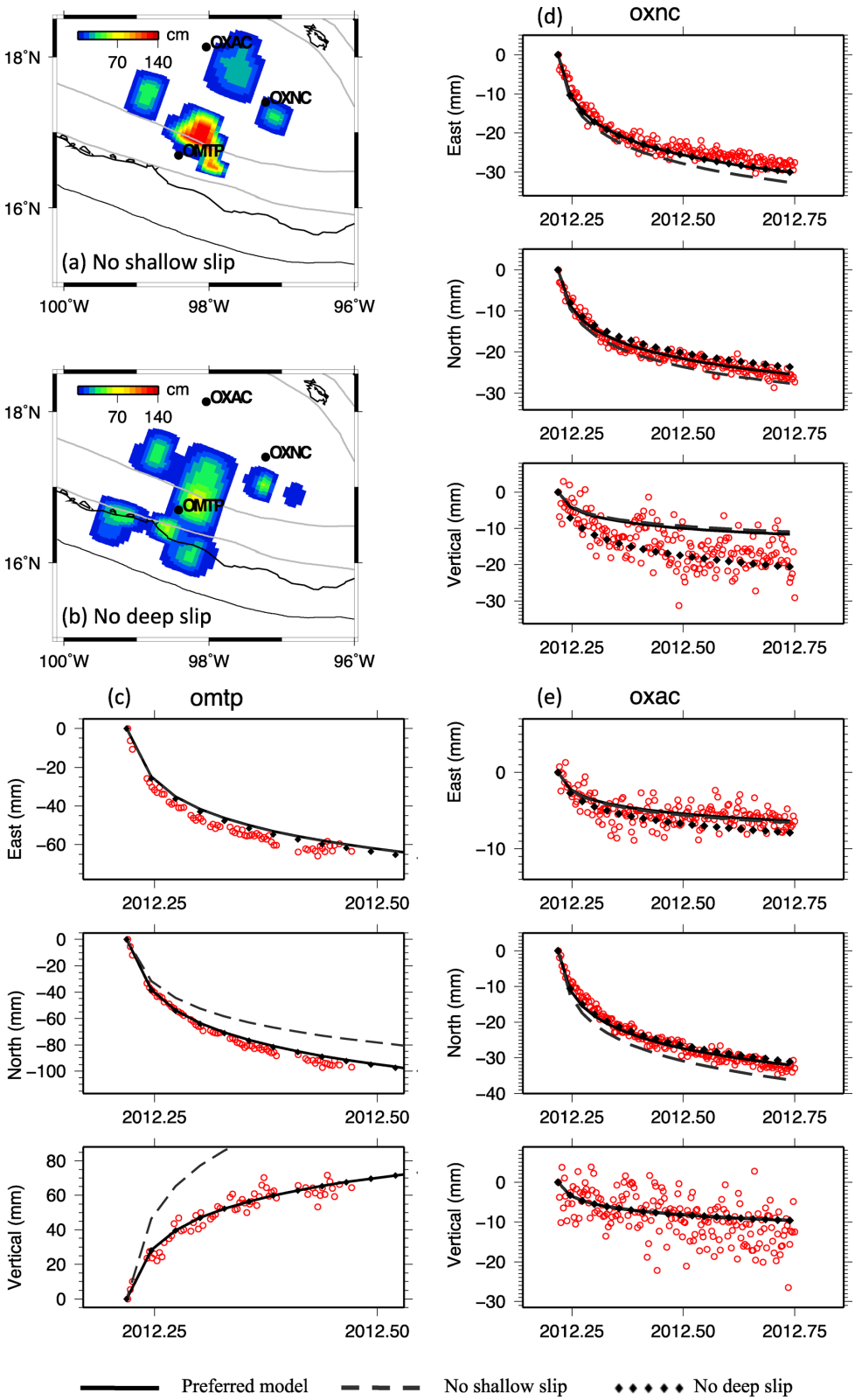

Figure 10. (a) Solution for distribution of fault afterslip for an inversion where any shallow afterslip (i.e. in the seismogenic zone) is forbidden. (b) Afterslip solution for an inversion where afterslip is disallowed at fault nodes deeper than 45 km depth, corresponding to farther than ∼150 km from the coast. (c–e) GPS horizontal and vertical daily position time-series for stations OMTP, OXNC and OXAC versus time-series predicted by the preferred afterslip model of Fig. 8 (solid line), and the no-shallow-slip (dashed line) and no-deep-slip (dotted line) models.

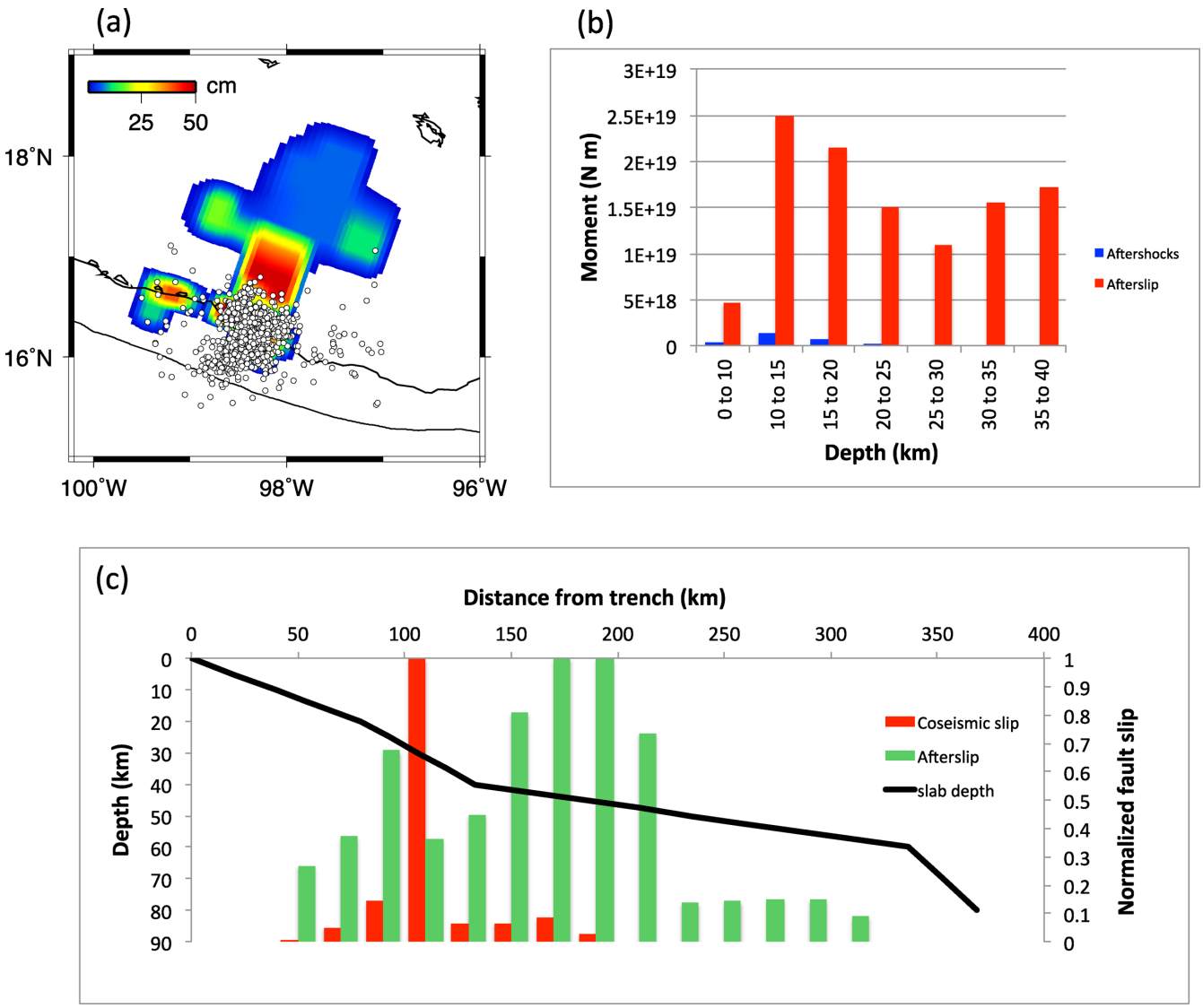

Figure 11. (a) Best-fitting afterslip solution with aftershocks (white circles) from March 21 to October 1. (b) Moment release by depth for aseismic afterslip (red bars) and aftershocks of $M \geq 4$ (blue bars). (c) Normalized amplitudes of coseismic slip and afterslip with distance inland from trench. Normalized amplitudes are determined by dividing each amplitude by the maximum amplitude along the profile. Amplitudes are averages for four fault nodes aligned parallel to the trench.

Ometepec earthquake relieved little or none of the elastic strain that has accumulated over the past few decades outboard from the coast.

7.3 Evidence for widespread afterslip

Fig. 12 summarizes our preferred solutions for slip during and after the Ometepec earthquake and for the 2011–2012 SSE that preceded the Ometepec earthquake (Graham *et al.* 2014). Together, they indicate that the Ometepec earthquake ruptured the plate interface at the leading edge of the westward propagating SSE, where small amounts of slip occurred in the weeks prior to the main shock. Although the Ometepec earthquake is interesting due to its close relationship in space and time to the 2011/2012 SSE, the most remarkable aspect of this otherwise unremarkable subduction earthquake is the geographic extent of its afterslip, which exceeds the area of the earthquake rupture zone by an order of magnitude or more (Figs 12 and 13). The transient deformation recorded at sites hundreds of km from the earthquake either requires that moderate afterslip occurred on the subduction interface far inland from the rupture zone or that large-amplitude afterslip was concentrated at shallower depths. Our tests for the location of the afterslip rule out the latter explanation and instead indicate that afterslip occurred at least 150 km inland beneath central Mexico and possibly as far as 220 km (Section 6.3.4).

Although we also considered viscous flow below central Mexico as a possible source of the transient post-seismic deformation, our modelling of the maximum likely viscoelastic response (Section 6.2) argues strongly against this possibility. The predicted viscoelastic deformation is surprisingly small, particularly in comparison to that estimated for larger earthquakes such as the 2004 $M = 9.2$ Sumatra earthquake (e.g. Pollitz *et al.* 2006; Hu & Wang 2012). We attribute the small viscoelastic deformation to the moderate magnitude of the Ometepec earthquake ($M_w = 7.5$) and the relatively thin mantle wedge (<10 km) above the nearly horizontal slab below central Mexico (Perez-Campos *et al.* 2008). These combine to predict

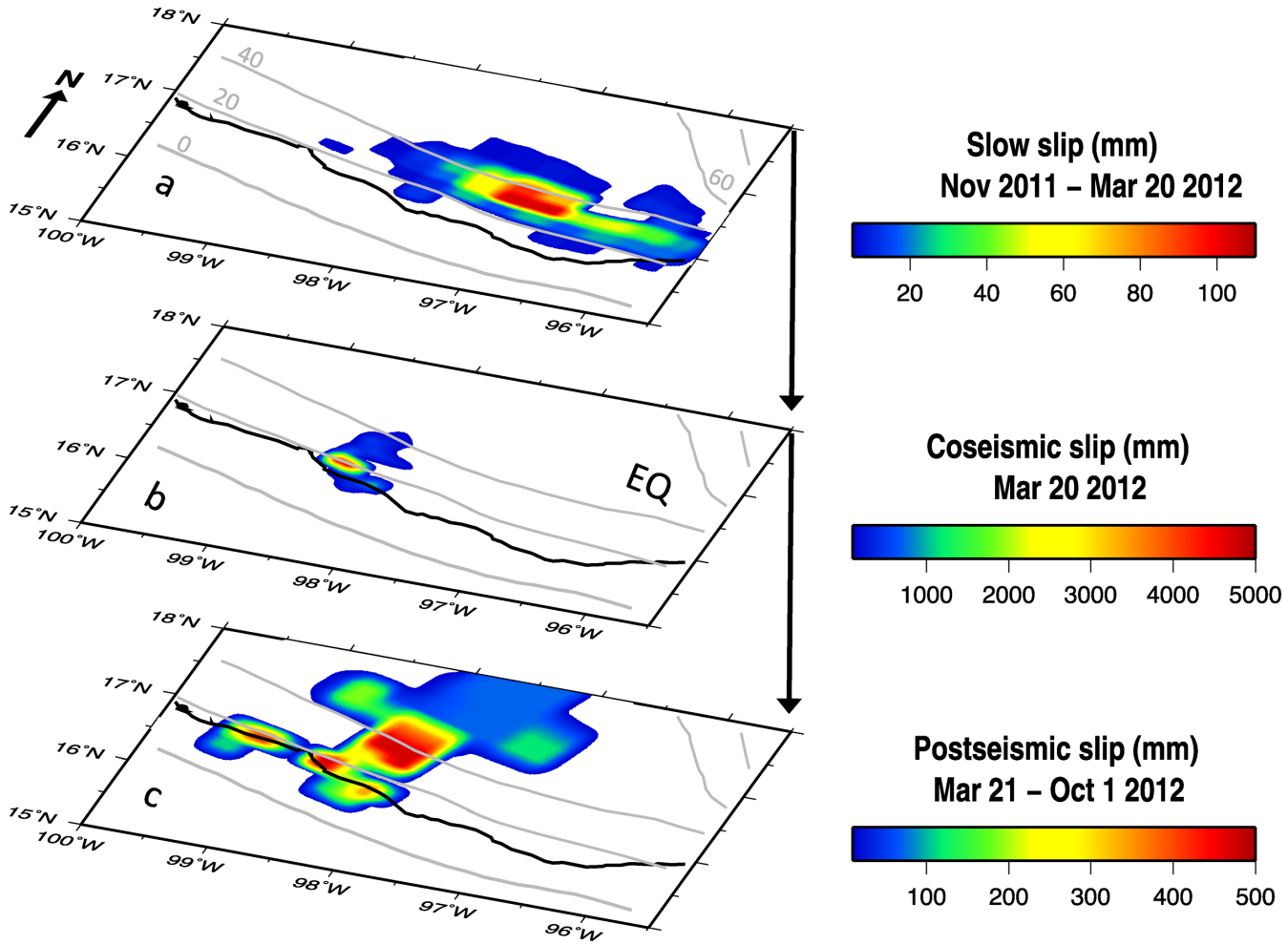

Figure 12. Space–time sequence of best-fitting models for (a) the 2011/2012 slow slip event (Graham *et al.* 2014), (b) the Ometepec earthquake on 2012 March 20 and (c) post-seismic afterslip. Grey lines show the subduction zone contours from the trench (depth of 0 km) to 60 km depth.

negligible viscoelastic deformation in central Mexico for viscosities the same as are used by Pollitz *et al.* (2006) to fit short-term (<1 yr) transient deformation for the 2004 Sumatra earthquake (5×10^{17} Pa s).

7.4 Role of afterslip in the earthquake cycle, central Mexico

As implied by Fig. 13, a complete understanding of the earthquake cycle along the seismically hazardous MSZ requires both an understanding of the processes that accumulate and release strain along the subduction interface, including how they vary along-strike and with depth, and viscoelastic deformation. Although viscoelastic relaxation of coseismic stresses undoubtedly occurs in the mantle wedge and lower crust below western Mexico, where the Rivera Plate subducts (Márquez-Azúa *et al.* 2002), our observations and modelling indicate that widespread afterslip instead dominated the short-term (<1 yr) post-seismic deformation in central Mexico. The distribution of afterslip clearly suggests that it relieved elastic strain both at seismogenic depths and along deeper, aseismic areas of the subduction interface (Fig. 13b).

Modelling of SSEs that have occurred below central Mexico indicates that the SSEs also affect large areas of the subduction interface inland from the Pacific coastline (Figs 13a and b; Lowry *et al.* 2001; Kostoglodov *et al.* 2003; Brudzinski *et al.* 2007; Larson *et al.* 2007; Correa-Mora *et al.* 2008, 2009; Vergnolle *et al.* 2010; Radiguet *et al.* 2012; Cavalie *et al.* 2013; Graham *et al.* 2014). The SSEs however have not extended farther than ~100 km inland from the coast (Fig. 13), equivalent to an approximate downdip depth limit of 40 km. In contrast, afterslip from the Ometepec earthquake extended at least 150 km inland and possibly as far as 220 km inland. Unlike slow slip, whose downdip limit appears to be defined by the occurrence of NVT (Payero *et al.* 2008; Brudzinski *et al.* 2010; Kostoglodov *et al.* 2010), afterslip also appears to extend at least as far and probably farther downdip (Fig. 13b).

That SSEs have been observed only to depths of ~40 km does not necessarily indicate that conditionally stable areas of the subduction interface below central Mexico are located solely above the ~40 km isodepth contour. Using afterslip as a proxy for conditionally stable areas of the plate interface, we instead speculate that conditionally stable regions of the subduction interface extend to at least the ~50 km isodepth contour. The Ometepec earthquake likely triggered aseismic slip at depths greater than those observed for SSEs because the velocity perturbation associated with the earthquake was presumably larger than the velocity perturbations that trigger SSEs.

Together, the evidence for afterslip and SSEs below central Mexico indicate that both relieve interseismic elastic strain that accumulates along the nearly horizontal subduction interface in this region. Whether NVT (Payero *et al.* 2008; Brudzinski *et al.* 2010;

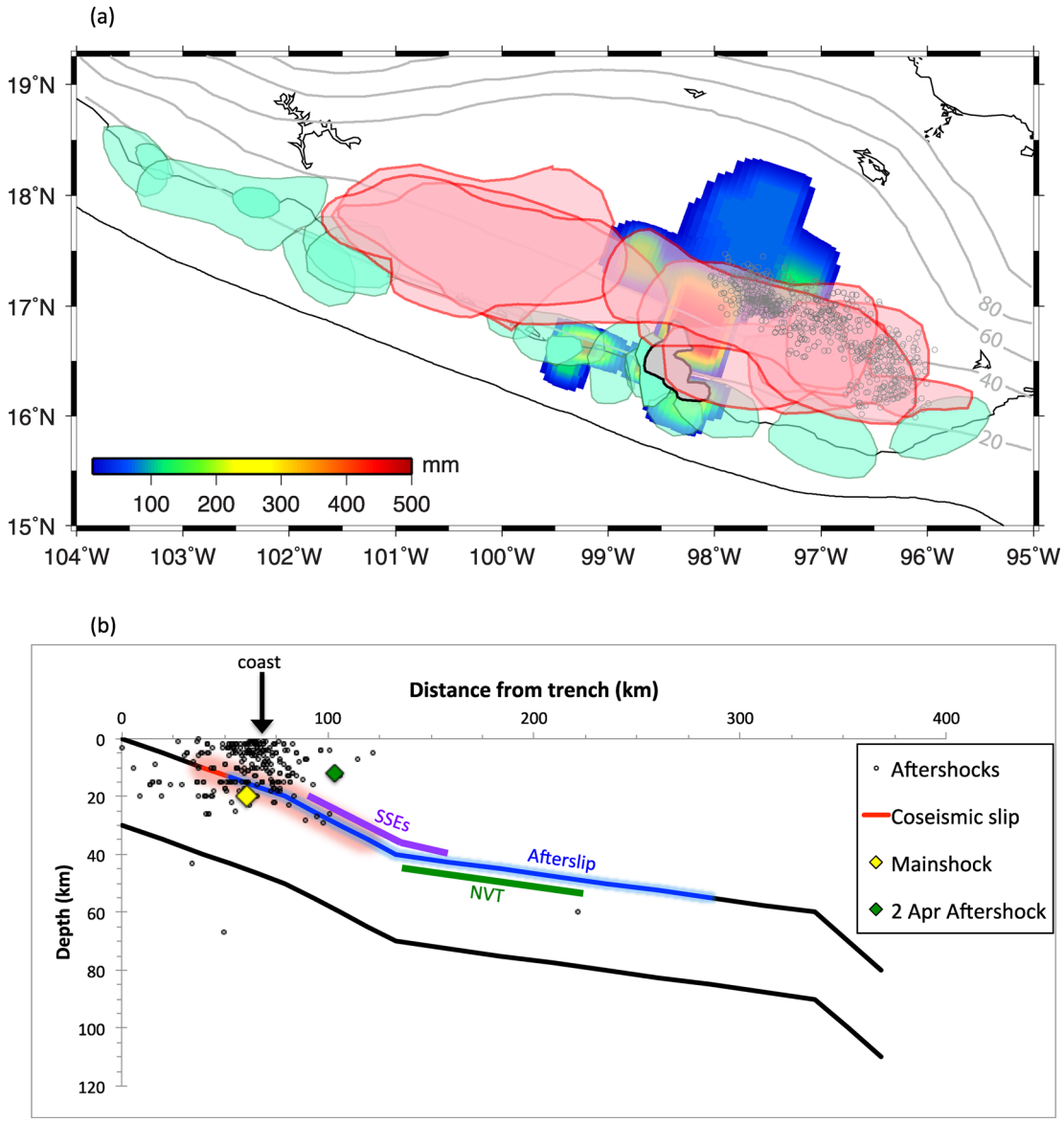

Figure 13. (a) Synthesis of locations for large thrust earthquakes along the Mexico subduction zone (cyan regions; after Franco *et al.* 2005), coseismic slip (black outline, grey centre) and afterslip for the 2012 March 20 earthquake (colour scale), and slow slip events below the states of Guerrero in 2001–2002,[1] 2006[2] and 2009–2010[2] and Oaxaca in 2004[3], 2006[2], 2007[2], 2008–2009[2], 2010–2011[2] and 2011–2012[4]. 60 mm slip contours are shown for the Guerrero slip events and 30 mm contours for slow slip events below Oaxaca. Non-volcanic tremor (NVT) locations are shown in open grey circles (Brudzinski *et al.* 2010). Subduction contours are shown in grey lines. (b) Cross section view of the processes in (a). Black lines show the subducting slab geometry for the transect in Fig. 4. Red and blues lines show coseismic slip and afterslip determined in this study, respectively. Purple and green lines show approximate SSE and NVT locations, respectively with respect to their trench normal locations. [1]Radiguet *et al.* 2012, [2]Graham 2013, [3]Correa-Mora *et al.* 2008, [4]Graham *et al.* 2014.

Kostoglodov *et al.* 2010) also relieves some elastic strain is unknown. Our results for afterslip in conjunction with slow slip and NVT raise several questions. Do these three processes interact in space and time? If so, how? Is the large-amplitude, widespread afterslip triggered by the 2012 Ometepec earthquake typical for this region? Does afterslip amplitude and extent depend at all on the current point in the slow slip cycle?

7.5 Implications for subduction mechanics in Mexico and elsewhere

Our coseismic and afterslip solutions fall within a wide range of earthquake/afterslip observations for other large subduction-thrust earthquakes. Along the MSZ, afterslip has been detected and modelled for only one other earthquake during the era of modern GPS, namely the $M = 8.0$ 1995 October 9 Colima-Jalisco earthquake along the Rivera Plate subduction interface. Post-seismic slip triggered by that earthquake extended ∼30 km inland from the coast to depths of ∼40 km (Hutton *et al.* 2001), a much smaller region than for the 2012 Ometepec earthquake. We suspect that this difference is a consequence of the steep versus shallow dips of the two plate interfaces and differences in their temperature versus depth profiles, which together influence where the transition occurs from velocity-weakening and hence seismogenic conditions to velocity-strengthening and hence aseismic conditions (Scholz 2002). The afterslips for the 1995 and 2012 earthquakes had cumulative

moments equal to 70 per cent (out to 1.5 yr; Hutton *et al.* 2001) and 140 per cent (out to 0.5 yr; this study) of their respective main shocks. Both thus relieved significant elastic strain across their plate interfaces downdip from their earthquake rupture zones.

Our evidence for significant afterslip in the region of high co-seismic slip (Section 6.3) is consistent with results reported by Johnson *et al.* (2012) from modelling of afterslip triggered by the 2011 Tohoku-Oki $M = 9$ earthquake. There, post-seismic GPS displacements are fit poorly unless afterslip is permitted to occur on areas of the subduction interface where historic ruptures occurred. Both cases are hard to explain via a physical model in which subduction interfaces consist of earthquake-prone asperities that are dominated by velocity-weakening frictional behaviour and velocity-strengthening areas prone to afterslip (Johnson *et al.* 2012). Our results also concur with theoretical (e.g. Kaneko *et al.* 2010) and observational evidence for heterogeneous frictional behaviour on nominally seismogenic areas of the subduction interface from modelling of interseismic coupling, coseismic rupture and fault afterslip in numerous other areas, including central Peru (Perfettini *et al.* 2010) and Chile (Chlieh *et al.* 2011; Vigny *et al.* 2011; Metois *et al.* 2012; Lin *et al.* 2013).

8 CONCLUSIONS

Modelling of continuous GPS observations from 2012 March 20 through October, comprising the coseismic and near-term post-seismic phases of the $M_w = 7.5$ Ometepec earthquake in southern Mexico show an earthquake source region with maximum slip of 4.7 m and geodetic moment of 1.4×10^{20} N·m ($M_w = 7.37$) in a 15–35 km depth range, consistent with an independently reported seismologic estimate. Results from modelling the SSE in 2011/2012 that preceded the Ometepec earthquake (Graham *et al.* 2014) indicate some overlap in space and time between the leading edge of the westward-migrating SSE and the downdip limit of the eventual Ometepec earthquake rupture. A forward model of the viscoelastic deformation for a Maxwell rheology lower crust and mantle wedge with assigned viscosities of 5×10^{17} Pa s driven by our coseismic slip solution predicts total horizontal deformation that is only 5–10 per cent of that measured within 6 months of the earthquake. The same model moreover predicts slow subsidence in areas near the rupture where GPS document rapid post-seismic uplift. Time-dependent modelling of the post-seismic deformation instead reveals that logarithmically decaying fault afterslip occurred along both the coseismic rupture area and areas of the nearly flat subduction interface to distances at least 150 km inland and more likely 220 km inland below central Mexico. By 6 months after the earthquake, the cumulative afterslip geodetic moment exceeded by ∼40 per cent the energy released by the 2012 earthquake. The cumulative moment of aftershocks was only ∼4 per cent that of the afterslip geodetic moment, thereby indicating that nearly all the afterslip occurred aseismically.

Overlap between the locations of earthquake afterslip and SSEs in 2011/2012 and previous years along the subduction interface below central Mexico suggests that both relieve deeply accumulating elastic strain, albeit at different times during the earthquake cycle. Our results suggest that much of central Mexico is underlain by areas of the subduction interface that are conditionally stable and thus can accumulate and release strain aseismically. Whereas the downdip limit of SSE appears to be bounded by areas of non-volcanic tectonic tremor (Brudzinski *et al.* 2010), the post-seismic afterslip extends well downdip from tremor locations in southern Mexico.

ACKNOWLEDGEMENTS

Funding was provided in part by National Science Foundation grant EAR-1114174 (DeMets). Graphics were prepared with Generic Mapping Tools software (Wessel and Smith 1991). Portions of the GPS network were supported by the CONACYT 84544, PAPIIT IN110611 grants (Mexico), and by the Agence Nationale de la Recherche (France) under the contract RA0000CO69 (G-GAP). We thank an anonymous reviewer, Shimon Wdowinski, and the associate editor for suggestions that significantly improved the original manuscript.

REFERENCES

Ali, S.T., 2014. Defmod—parallel multiphysics finite element code for modeling crustal deformation during the earthquake/rifting cycle (preprint, arXiv:1402.0429).

Altamimi, Z., Collilieux, X. & Métivier, L., 2011. ITRF2008: an improved solution of the international terrestrial reference frame, *J. Geod.,* **85,** 457–473.

Anderson, J.G., Singh, S.K., Espindola, J.M. & Yamamoto, J., 1989. Seismic strain release in the Mexican subduction thrust, *Phys. Earth planet. Inter.,* **58,** 307–322.

Brudzinski, M., Cabral-Cano, E., Correa-Mora, F., DeMets, C. & Márquez-Azúa, B., 2007. Slow slip transients along the Oaxaca subduction segment from 1993 to 2007, *Geophys. J. Int.,* **171,** 523–538.

Brudzinski, M.R., Hinojosa-Prieto, H.R., Schlanser, K.M., Cabral-Cano, E., Arciniega-Ceballos, A., Diaz-Molina, O. & DeMets, C., 2010. Non-volcanic tremor along the Oaxaca segment of the Middle America subduction zone, *J. geophys. Res.: Solid Earth,* **115,** B00A23, doi: 10.1029/2008JB006061.

Burgmann, R. & Dresen, C., 2008. Rheology of the lower crust and upper mantle: evidence from rock mechanics, geodesy, and field observations, *Annu. Rev. Earth planet. Sci.,* **36,** 531–567.

Cavalie, O., Pathier, E., Radiguet, M., Vergnolle, M., Cotte, N., Walpersdorf, A., Kostoglodov, V. & Cotton, F., 2013. Slow slip event in the Mexican subduction zone: evidence of shallower slip in the Guerrero seismic gap for the 2006 event revealed by the joint inversion of InSAR and GPS data, *Earth planet. Sci. Lett.,* **367,** 52–60.

Chlieh, M. & Perfettini, H. many others. 2011. Interseismic coupling and seismic potential along the Central Andes subduction zone, *J. geophys. Res.,* **116,** B12405, doi:10.1029/2010JB008166.

Correa-Mora, F., DeMets, C., Cabral-Cano, E., Diaz-Molina, O. & Márquez-Azua, B., 2009. Transient deformation in southern Mexico in 2006 and 2007: evidence for distinct deep-slip patches beneath Guerrero and Oaxaca, *Geochem. Geophys. Geosyst.* **10,** Q02S12, doi:10.1029/2008GC002211.

Correa-Mora, F., DeMets, C., Cabral-Cano, E., Márquez-Azúa, B. & Diaz-Molina, O., 2008. Interplate coupling and transient slip along the subduction interface beneath Oaxaca, Mexico, *Geophys. J. Int.,* **175,** 269–290.

DeMets, C., Gordon, R.G. & Argus, D.F., 2010. Geologically current plate motions, *Geophys. J. Int.,* **181,** 1–80.

Ekström, G., Nettles, M. & Dziewonski, A.M., 2012. The global CMT project 2004–2010: centroid-moment tensors for 13,017 earthquakes, *Phys. Earth planet. Inter.,* **200–201,** 1–9. doi:10.1016/j.pepi.2012.04.002.

Graham, S.E., 2013, Earthquake cycle deformation in Mexico and Central America constrained by GPS: implications for coseismic, postseismic, and slow slip, *PhD dissertation,* University of Wisconsin-Madison, 182 p.

Graham, S.E. *et al.*, 2014. GPS constraints on the 2011/12 Oaxaca slow slip event that preceded the 20 March 2012 Ometepec earthquake, southern Mexico, *Geophys. J. Int.,* **197**(3), 1593–1607.

Hu, Y. & Wang, K., 2012. Spherical-Earth finite element model of short-term postseismic deformation following the 2004 Sumatra earthquake, *J. geophys. Res.,* **117,** B05404, doi:10.1029/2012JB009153.

Hutton, W., DeMets, C., Sánchez, O., Suárez, G. & Stock, J., 2001. Slip kinematics and dynamics during and after the 1995 October 9 Mw = 8.0

Colima–Jalisco earthquake, Mexico, from GPS geodetic constraints, *Geophys. J. Int.,* **146,** 637–658.

Johnson, K.M., Fukuda, J.i. & Segall, P., 2012. Challenging the rate-state asperity model: afterslip following the 2011 M9 Tohoku-oki, Japan, earthquake, *Geophys. Res. Lett.,* **39,** L20302, doi:10.1029/2012GL052901.

Kaneko, Y., Avouac, J.-P. & Lapusta, N., 2010. Towards inferring earthquake patterns from geodetic observations of interseismic coupling, *Nat. Geosci.,* **3,** doi:10.1038/NGEO843.

Kim, Y., Clayton, R.W. & Jackson, J.M., 2010. Geometry and seismic properties of the subducting Cocos plate in central Mexico, *J. geophys. Res.,* **115,** B06310, doi:10.1029/2010JB006942.

Kostoglodov, V., Singh, S.K., Santiago, J.A., Franco, S.I., Larson, K.M., Lowry, A.R. & Bilham, R., 2003. A large silent earthquake in the Guerrero seismic gap, Mexico, *Geophys. Res. Lett.,* **30,** 1807, doi:10.1029/2003GL017219.

Kostoglodov, V., Husker, A., Shapiro, N.M., Payero, J.S., Campillo, M., Cotte, N. & Clayton, R., 2010. The 2006 slow slip event and nonvolcanic tremor in the Mexican subduction zone, *Geophys. Res. Lett.,* **37,** L24301, doi:10.1029/2010GL045424.

Larson, K.M., Kostoglodov, V., Miyazaki, S.i. & Santiago, J.A.S., 2007. The 2006 aseismic slow slip event in Guerrero, Mexico: new results from GPS, *Geophys. Res. Lett.,* **34,** L13309, doi:10.1029/2007GL029912.

Lin, Y.N. *et al.*, 2013. Coseismic and postseismic slip associated with the 2010 Maule earthquake, Chile: characterizing the Arauco Peninsula barrier effect, *J. geophys. Res.,* **118,** 1–18.

Lowry, A., Larson, K., Kostoglodov, V. & Bilham, R., 2001. Transient fault slip in Guerrero, southern Mexico, *Geophys. Res. Lett.,* **28,** 3753–3756.

Marone, C.J., Scholtz, C.H. & Bilham, R., 1991. On the mechanics of earthquake afterslip, *J. geophys. Res.: Solid Earth,* **96,** 8441–8452.

Márquez-Azúa, B. & DeMets, C., 2003. Crustal velocity field of Mexico from continuous GPS measurements, 1993 to June 2001: implications for the neotectonics of Mexico, *J. geophys. Res.,* **108,** 2450, doi:10.1029/2002JB002241.

Márquez-Azúa, B., DeMets, C. & Masterlark, T., 2002. Strong interseismic coupling, fault afterslip, and viscoelastic flow before and after the Oct. 9, 1995 Colima-Jalisco earthquake: continuous GPS measurements from Colima, Mexico, *Geophys. Res. Lett.,* **29,** 122-121–122-124.

McCaffrey, R., 2009. Time-dependent inversion of three-component continuous GPS for steady and transient sources in northern Cascadia, *Geophys. Res. Lett.,* **36,** L07304, doi:10.1029/2008GL036784.

Metois, M., Socquet, A. & Vigny, C., 2012. Interseismic coupling, segmentation, and mechanical behavior of the central Chile subduction zone, *J. geophys. Res.,* **117,** B03406, doi:10.1029/2011JB008736.

Okada, Y., 1992. Internal deformation due to shear and tensile faults in a half-space, *Bull. seism. Soc. Am,* **82,** 1018–1040.

Pacheco, J.F. & Singh, S.K., 2010. Seismicity and state of stress in Guerrero segment of the Mexican subduction zone, *J. geophys. Res.: Solid Earth,* **115,** B01303, doi:10.1029/2009JB006453.

Payero, J.S., Kostoglodov, V., Shapiro, N., Mikumo, T., Iglesias, A., Pèrez-Campos, X. & Clayton, R.W., 2008. Nonvolcanic tremor observed in the Mexican subduction zone, *Geophys. Res. Lett.,* **35,** L07305, doi:10.1029/2007gl032877.

Pegler, G. & Das, S., 1996. Analysis of the relationship between seismic moment and fault length for large crustal strike-slip earthquakes between 1977–92, *Geophys. Res. Lett.,* **23,** 905–908.

Pérez-Campos, X. *et al.*, 2008. Horizontal subduction and truncation of the Cocos Plate beneath central Mexico, *Geophys. Res. Lett.,* **35,** L18303, doi:10.1029/2008GL035127.

Perfettini, H. & Avouac, J.-P., 2004. Postseismic relaxation driven by brittle creep: a possible mechanism to reconcile geodetic measurements and the decay rate of aftershocks, application to the Chi-Chi earthquake, Taiwan, *J. geophys. Res.,* **109,** B02304, doi:10.1029/2003JB002488.

Perfettini, H. *et al.*, 2010. Seismic and aseismic slip on the Central Peru megathrust, *Nature,* **465,** 78–81.

Pollitz, F.F., Bürgmann, R. & Banerjee, P., 2006. Post-seismic relaxation following the great 2004 Sumatra-Andaman earthquake on a compressible self-gravitating Earth, *Geophys. J. Int.*, **167**, 397–420.

Radiguet, M., Cotton, F., Vergnolle, M., Campillo, M., Walpersdorf, A., Cotte, N. & Kostoglodov, V., 2012. Slow slip events and strain accumulation in the Guerrero gap, Mexico, *J. geophys. Res.: Solid Earth,* **117,** B04305, doi:10.1029/2011JB008801.

Rousset, Baptiste, 2013. Interseismic deformation on the Mexican Subduction Zone seen by GPS: from small slow slip events to long term deformation. *M.S.* (de la Terre et de l'Univers - option Terre Solide) Université Joseph Fourier, Grenoble.

Scholz, C.H., 2002. *The Mechanics of Earthquakes and Faulting,* Cambridge Univ. Press.

Skinner, S.M. & Clayton, R.W., 2011. An evaluation of proposed mechanisms for slab flattening in central Mexico, *Pure appl. Geophys.*, **168**(8-9), 1461–1474.

Song, T.-R.A., Helmberger, D.V., Brudzinski, M.R., Clayton, R.W., Davis, P., Pérez-Campos, X. & Singh, S.K., 2009. Subducting slab ultra-slow velocity layer coincident with silent earthquakes in southern Mexico, *Science,* **324,** 502–506.

Suárez, G. & Sánchez, O., 1996. Shallow depth of seismogenic coupling in southern Mexico: implications for the maximum size of earthquakes in the subduction zone, *Phys. Earth planet. Inter.,* **93,** 53–61.

Suárez, G. & Albini, P., 2009. Evidence for great tsunamigenic earthquakes (M 8.6) along the Mexican Subduction Zone, *Bull. seism. Soc. Am.,* **99,** 892–896.

Universidad Nacional Autonoma de Mexico Seismology Group, 2013. Ometepec-Pinotepa Nacional, Mexico earthquake of 20 March 2012 (M_w7.5): a preliminary report, *Geof. Int.,* **52–2,** 173–196.

Vergnolle, M., Walpersdorf, A., Kostoglodov, V., Tregoning, P., Santiago, J.A., Cotte, N. & Franco, S.I., 2010. Slow slip events in Mexico revised from the processing of 11 year GPS observations, *J. geophys. Res.,* **115,** B08403, doi:10.1029/2009JB006852.

Vigny, C. *et al.*, 2011. The 2010 M_w 8.8 Maule megathrust earthquake of central Chile, monitored by GPS, *Science,* **332,** 1417–1421.

Wang, K., Hu, Y. & He, J., 2012. Deformation cycles of subduction earthquakes in a viscoelastic Earth, *Nature,* **484,** 327–332.

Wessel, P. & Smith, W.H.F., 1991. Free software helps map and display data, *EOS, Trans. Am. geophys. Un.,* **72,** 455–473.

Yamamoto, J., Gonzalez-Moran, T., Quintanar, L., Zavaleta, A.B., Zamora, A. & Espindola, V.H., 2013. Seismic patterns of the Guerrero-Oaxaca, Mexico region, and its relationship to the continental margin structure, *Geophys. J. Int.,* **192,** 375–389.

Zumberge, J.F., Heflin, M.B., Jefferson, D.C., Watkins, M.M. & Webb, F.H., 1997. Precise point positioning for the efficient and robust analysis of GPS data from large networks, *J. geophys. Res.: Solid Earth,* **102,** 5005–5017.

SUPPORTING INFORMATION

Additional Supporting Information may be found in the online version of this article:

Figure S1. Resolution tests for checkerboard starting model (a) and simulated afterslip model (b). Results from inversions of noisy synthetic displacements created for the two starting models at the locations of existing GPS sites in central Mexico are shown in (c), (d) and (e). The inversion of the checkerboard model was completed for two sets of station distributions: stations used in the coseismic slip inversion (c) and stations used in the post-seismic inversion (e). The inversion of the simulated afterslip model (d) was completed using the post-seismic station distribution.

Figure S2. Trade-off between smoothing value and variance of the slip solution for inversions of (a) the coseismic offsets and (b) the post-seismic GPS position time-series. The smoothing criterion we use for the coseismic inversion (a) encourages slip to concentrate around a central area on the fault. Larger smoothing values correspond to slip models that encourage a greater concentration of slip around a centroid. Smaller smoothing values allow more variation

in slip along the subduction interface. We selected smoothing values to optimize the trade-off between the two. For the post-seismic inversion (b), we use the gradient smoothing option in TDEFNODE where neighbouring nodes are penalized for large gradients in slip magnitude.

Figure S3. (a) Best afterslip solution for an assumed 2-D Gaussian source. White and red vectors show the observed and predicted surface displacements integrated over the first 6 months of post-seismic movement. The cumulative offsets (white) were not used to constrain the model, and instead show an independent comparison to deformation predicted by the best fit to the time-series. Fits of 2-D Gaussian model to daily positions for sites OMTP (b), OXAC (c) and OXNC (d), north, east and vertical components.

Figure S4. Fits to all of the time-series for the best-fitting post-seismic deformation model. Red dots are data points and black lines are model predictions. (http://gji.oxfordjournals.org/lookup/suppl/doi:10.1093/gji/ggu167/-/DC1)

Please note: Oxford University Press is not responsible for the content or functionality of any supporting materials supplied by the authors. Any queries (other than missing material) should be directed to the corresponding author for the article.